LONG-SLIT OPTICAL SPECTROSCOPY OF EMISSION-LINE NEBULAE IN RADIO GALAXIES: THE DATA

STEFI A. BAUM¹
Netherlands Foundation for Research in Astronomy
TIMOTHY HECKMAN^{1,2,3}
Johns Hopkins University

AND

WIL VAN BREUGEL

Lawrence Livermore Laboratories and University of California at Berkeley Received 1989 December 8; accepted 1990 March 7

ABSTRACT

We present the results from an extensive program of long-slit spectroscopy at multiple position angles of the extended emission-line nebulae around 19 radio galaxies. These observations were conducted in order to study the kinematics and line ratios in the nebulae. In this, the first of two papers, we present the data.

In general, we do not find *strong* gradients in the H α to [N II] $\lambda 6583$ ratio within a source. Often there is a slight decline in this ratio with distance from the nucleus, but there are also a few cases in which the ratio rises rapidly in the very extended emission-line gas.

In some sources, the gas appears to be in rotation about the galaxy nucleus, with measured rotational velocities ranging from 100 to 325 km s⁻¹, and apparent flattenings of the rotation curves occurring at distances from 0.1 to 8 kpc from the nucleus. Frequently, the rotation curves appear to be asymmetrically situated with respect to the nuclear line-emitting gas, showing offsets of ~ 1 kpc, or ~ 60 km s⁻¹, with respect to the nuclear gas. The shift of the nuclear velocity from the mean velocity of the emission-line gas is sometimes in the sense of a redshift and sometimes in the sense of a blueshift.

In other sources we find that the emission-line gas within several kiloparsecs of the nucleus shows no evidence for rotation, but the velocities of the gas farther out are positive on one side of the nucleus and negative on the other. Finally, in others we find no evidence for rotational gradients across the nucleus, but observe either all velocities within 50 km s⁻¹ of the velocity of the nuclear emission-line gas, or velocities which vary greatly from the nuclear velocities, but in an unsystematic manner.

Measured line widths vary from 200 to 600 km s⁻¹ (FWHM) on the nucleus. The line widths typically fall with increasing distance from the nucleus, although there are several potentially interesting exceptions to this pattern. Finally, in those sources where there is extended emission-line gas along the radio source axis we have been able to look for evidence that the gas and the radio source are interacting. While kinematic signs of such an interaction are present in a few sources, others show no evidence that the gas has been disturbed by the passage of the radio jet or the presence of backflowing radio plasma. These results will be discussed in more detail in the forthcoming analysis paper.

Subject headings: galaxies: internal motions — nebulae: H II regions — radio sources: galaxies

I. INTRODUCTION

In the past several years, narrow-band imaging surveys of radio galaxies have shown that radio galaxies frequently contain optical line-emitting gas ($T \sim 10^4$ K) which is extended on scales of kiloparsecs to tens of kiloparsecs (Fosbury 1986, and references therein, Hansen, Noorgard-Nielsen, and Jorgensen 1987; Baum *et al.* 1988, hereafter Paper I; McCarthy 1988). By studying the properties of this gas we can hope to unravel clues to such things as the nature of the

central engine responsible for the activity in these galaxies, the origin of the observed activity, the physics of the outflowing radio plasma, and the physical properties and recent histories of the host elliptical galaxies. In several previous papers (Baum and Heckman 1989a, hereafter Paper I; Baum and Heckman 1989b), we have described the results of a program of narrow-band optical, broad-band optical, and VLA radio imaging of a representative sample of 42, relatively nearby, radio galaxies. In this paper we present the results of an extensive program of long-slit optical spectroscopy of the extended regions of emission-line gas found in 19 of these galaxies. Spectroscopic results on another four radio sources from the original sample (those at the centers of rich clusters suspected of having "cooling flows") have already been presented elsewhere (Heckman et al. 1989).

³Space Telescope Science Institute.

¹Visiting Astronomer, Kitt Peak National Observatory, operated by AURA, Inc., under contract to the National Science Foundation.

²On leave from University of Maryland, College Park, MD 20742.

In § II, we describe the details of the observations. Section III describes the data reduction and parameter extraction. In § IV the results are presented, and in § V individual sources are described. Finally, in § VI we summarize our findings. A detailed analysis of the results for the sample as a whole will be presented in a forthcoming paper (Paper II).

II. OBSERVATIONS

We used the Ritchey-Chrétien spectrograph with a Texas Instrument CCD on NOAO's 4 m Mayall telescope at Kitt Peak to obtain long-slit optical spectroscopy at multiple position angles of the extended emission-line gas around a sample of 23 powerful radio galaxies. These were objects with extended emission-line regions found from narrow-band imaging of a representative sample of relatively nearby radio galaxies as described in Paper I. The details of the observations are given in Table 1, where we list the slit positions obtained, the integration time per slit position, the date of the observations, and a comment on the observing conditions for each slit position obtained.

We used the Baush and Lamb 420 grating blazed at 7500 Å in first order, in conjunction with a blocking filter, to prevent light from the higher orders from entering the CCD. The grating is ruled with 600 lines mm⁻¹, yielding a spectral resolution of 0.95 Å per single pixel. The wavelength axis of the chip runs vertically, the direction along which the chip is read out. We employed a slit width of $\sim 300 \ \mu \text{m}$ ($\sim 2''$) and performed on-chip summation of adjacent columns and rows of the CCD prior to readout in order to minimize the effect of readout noise. In this mode, the CCD has 400 columns and rows. The resultant spectral resolution is ~3.8 Å (FWHM), and the total spectral coverage is ~ 700 Å. The spatial scale of each "big" pixel is 0".86. We have sacrificed spatial resolution for signal to noise, since we are interested in mapping extended gas. The total "useful" length of the slit is ~ 320 pixels, or 4.5. We note that for the two sources 3C 98 and 3C 192, on-chip summation was performed only in the spatial direction.

For each galaxy observed we adjusted the tilt of the grating so that the $H\alpha$ $\lambda6562$ line was centered in the middle of the chip. We observed a quartz lamp, in order to flatfield the images, and a helium-neon-argon lamp, in order to calibrate the wavelength scale of the images, prior to and following each change of the slit position angle, the grating tilt, or both. During the 1987 April observing run, we also obtained a series of between 10 and 20 bias (i.e., unexposed) frames, which were then averaged together to produce the bias frame used in the reduction of the images (see below).

Finally, we note that the Texas Instrument CCDs are subject to charge transfer problems at low light levels. During the 1987 April observations, we were able to "preflash" the chip (i.e., expose the chip to light prior to observing, in order to raise the base level of charge on the chip to ~ 25 ADUs so that the charge is efficiently transferred). However, in the 1986 November observing run, mechanical difficulties made preflashing impossible. The charge transfer problem manifests itself in the sky-subtracted images from November, where the night-sky lines appear to be undersubtracted in the region of the chip where the galaxy continuum is strong.

III. REDUCTION OF LONG-SLIT SPECTRA

The data were reduced using the IRAF software package. For the data taken in 1986 November, the DC electrical offset of the CCD (i.e., the bias) was removed on a row-by-row basis; the 30 unilluminated columns in the bias region of the chip were averaged together, and a cubic spline of 50 elements was fitted to the row-by-row variation of the bias. For the spectra taken in 1987 April, the average DC electrical offset of the chip was removed from each frame (including the bias frame) using the average value from the 30 column unilluminated region of the chip, and then the low spatial frequency variations in the zero-point level across the chip were removed by subtracting the bias frame.

Each frame was flatfielded using the accompanying quartz lamp exposures. However, the quartz lamp does not illuminate the slit in the same way as does the sky, and the intensity of the quartz lamp is a function of wavelength. Therefore, the large-scale structure in the quartz frames must be removed before they can be used to correct the source images for the pixel-to-pixel variations in the response of the CCD. A two-dimensional cubic spline was fitted to each 50×50 pixel region of the quartz frame, the quartz frame was divided by the fit and normalized, thereby producing a quartz frame which retained any small-scale structure, but from which the large-scale structure had been removed. The normalized flat-field frame was then divided into the appropriate source frame.

Next, the illumination of the slit by the sky was determined for each source image. A low-order (order three or four) polynomial was fitted to the source-free region of the slit, within five wavelength bins (i.e., the chip was divided into five regions in the vertical direction, and the pixel values were averaged in y for each value of x). The fits were then interpolated to produce a two-dimensional profile of the slit response which is normalized at the center of the slit. Each source frame was then divided by its slit profile.

A linear wavelength scale was then affixed to each source frame. To do this, a polynomial of order five to nine was fitted to identified lines in the helium-neon-argon comparison frames for each observation. Each identified helium, neon, or argon line was then traced along the slit, a twodimensional polynomial was fitted to the lines, and the images were transformed to correct for the distortion. To correct for S-distortion (i.e., the displacement of a point source from a constant x-value, as a function of v), the location of the galaxy nucleus was traced as a function of λ , a polynomial fitted to the tracing, and the image transformed to correct for the distortion. Typically, the point source shifted only 0".25 (or one-third of a pixel) from end to end. The final result of the coordinate transformation is to produce an image which has a constant scale of angstroms per pixel along the chip, a fixed zero point to the wavelength scale, and from which any S-distortion has been removed.

Finally, we subtracted the sky emission from each source image, by fitting a low-order (typically degree two) polynomial to the nonsource regions of the slit. Typically, the regions along the slit closest to the source were used to fit the sky, but care was taken to avoid any regions which might contain emission lines from the source.

LONG-SLIT SPECTROSCOPY OF RADIO GALAXIES

TABLE 1
Log of Optical Spectroscopy

Source	Slit Position	Slit Angle	Integration Time (s)	Date Obs	Comments
3C 29	Nucleus	12°	1800	1986 Nov	Clouds
3C 33	Nucleus	19°	1800	1986 Nov	0.0000
3C 63	Nucleus	90°	1800	1986 Nov	
3C 78	Nucleus	60°	1800	1986 Nov	
30 70	Nucleus	120°	1800	1986 Nov	
	Nucleus	180°	1800	1986 Nov	
3C 88	Nucleus	30°	1800	1986 Nov	
50 00	Nucleus	90°	1800	1986 Nov	
	Nucleus	150°	1800	1986 Nov	
3C 98	Nucleus	163°	1800	1986 Nov	
30 70	2".5 east	163°	1800	1986 Nov	
	2".5 west	163°	1800	1986 Nov	
	5".0 east	163°	1800	1986 Nov	
	5".0 west	163°	1800	1986 Nov	
PKS 0634-206	Nucleus	85°	1800	1986 Nov	
1 KS 0054-200	21".0 north	85°	1800	1986 Nov	
	Nucleus	124°	1800	1986 Nov	
PKS 0745-191*	Nucleus	112°	1800	1986 Nov	
1 K3 0/43-171	Nucleus	156°	1800	1986 Nov	
3C 192	Nucleus	130 145°	1800	1986 Nov	
JC 192	10".5 west	15°	1800	1986 Nov	
	Nucleus	0°	300	1986 Nov	
	4".0 east	0°	1800	1986 Nov	
3C 196.1	Nucleus	52°	1800	1986 Nov	
3C 218*	Nucleus	0°	1055		Clouds
3C 227	Nucleus	38°	1800	1987 Apr 1986 Nov	Clouds
oc 227	Nucleus	36 121°	1800	1986 Nov	
	5".2 south	121°			
	27".0 east	121 172°	1800 1200	1986 Nov 1986 Nov	
3C 264	Nucleus	85°	1800		Clouds
3C 204		175°		1987 Apr	
20 272 1	Nucleus	85°	1243	1987 Apr	Clouds
3C 272.1	Nucleus Nucleus	65 175°	1800 924	1987 Apr	Clouds
20.274*				1987 Apr	Ciouas
3C 274*	2".4 north	128°	1800	1987 Apr	
20.205	13″.6 north	128° 95°	1800	1987 Apr	
3C 285	Nucleus		1800	1987 Apr	Cl. I
DIZC 1245 + 125	Nucleus	140°	1500	1987 Apr	Clouds
PKS 1345+125	Nucleus	60°	1800	1987 Apr	CI I
3C 317*	Nucleus	78°	1596	1987 Apr	Clouds
20,252	11".3 east	135°	1800	1987 Apr	
3C 353	Nucleus	160°	1800	1987 Apr	
3C 403	Nucleus	110°	1200	1987 Apr	
20. 405	Nucleus	20°	1200	1987 Apr	
3C 405	Nucleus	160°	600	1987 Apr	
	2".0 east	160°	600	1987 Apr	
26. 422	2".0 west	160°	600	1987 Apr	
3C 433	Nucleus	129°	1800	1986 Nov	
3C 442	Nucleus	126°	1800	1986 Nov	
	Nucleus	36°	1800	1986 Nov	

Col. (1).—Source name. An asterisk indicates that the data are presented in Heckman et al.

Numbers were extracted from the calibrated spectra using the SPLOT task in the IRAF package. This task fits and deblends Gaussians plus a linear baseline to a line or line complex. The baseline is user-determined, but the peak, centroid, and width of the Gaussian are free parameters of the fitting routine. In the case of deblending multiple lines, the program allows the user to fix the separation between lines and to specify that the widths of the lines be the same, although we rarely employed this option. Thus, the program returns a peak flux, an integrated flux, a line width (FWHM), and a line centroid for each line measured. The quoted line widths have been corrected for the spectral resolution of the

Col. (2).—Split position. Offsets are from the galaxy nucleus.

Col. (3).—Slit angle in degrees counterclockwise from due north.

Col. (4).—Integration time in seconds.

Col. (5).—Date of observation.

Col. (6).—Comments as to weather conditions. No comment means clear skies.

392 BAUM ET AL.

instrument (as measured with night-sky lines) via the Gaussian "quadrature" technique $(w = [w_{obs}^2 - w_{nt-sky}^2]^{1/2})$ and were corrected to the rest frame of the host galaxy. For each spectrum, we determined, where possible, the parameters of the following lines: [O I] $\lambda 6300.3$; H α $\lambda 6562.8$; [N II] $\lambda\lambda6548.1$, 6583.4; [S II] $\lambda\lambda6716.4$, 6730.8. When the H α lines had a broad component, the line widths and centroids were determined only from the forbidden lines. A flux-weighted mean line width (in km s⁻¹) and a flux-weighted mean line centroid (in km s⁻¹) were determined at each spatial pixel location in each spectra in which there was adequate signal to noise to measure one or more lines. The flux weighting was done as follows: Given N measured lines for a given parameter p, the flux-weighted mean value of p was defined to be $p_{\text{mean}} = \sum (p_i/F_i)/\sum (1/F_i)$, where p_i and F_i are, respectively, the value of the parameter p as determined from the ith line and the flux in the ith line, and the sum is over the N measured lines. Under the assumption that, for a given pixel, the lines originate under the same physical conditions, the differences in velocity width and velocity centroid determined for the set of (independently) measured lines can then also be used to estimate the nonsystematic errors in the determination of these properties. Thus, the accompanying estimated error in the determination of the mean is

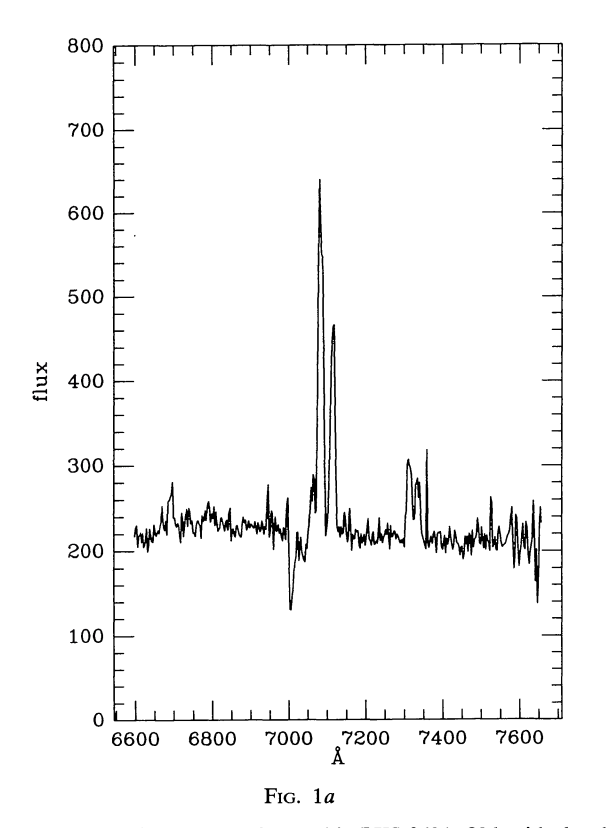
$$\sigma^{2} = \Sigma \left[F_{i} \times (p_{i} - p_{\text{mean}})^{2} \right] / \left[(N - 1) \times \Sigma(F_{i}) \right],$$

where N is the total number of lines measured. Where more

than one line is measurable and the line strengths are of order 500 or more, typical errors in the mean are less than 20 km s⁻¹ for the line centroid, and $\sim 20-50$ km s⁻¹ for the line widths. (Note the spectra are not flux calibrated. The CCD chip employed has a gain of ~ 4.1 electrons per ADU, and the values quoted are in ADU.) Similarly, the measured ratio of [N II] $\lambda 6583$ to [N II] $\lambda 6548$, which is fixed by microphysics at ~ 3 , can be used to estimate the accuracy of the line ratios. The percent error on the determination of the [N II] $\lambda 6583$ to [N II] $\lambda 6548$ ratio can be as high as 30% but is typically in the 5%-20% range for line strengths of order 500 or more. A typical spectrum is shown in Figure 1.

IV. RESULTS

We present the fluxes and velocities of the emission-line gas in Tables 2–42, with one table for each position angle of the slit for each source. Each table is arranged as follows. Column (1) gives the increment along the slit in pixels from zero, where zero is the location of the galaxy nucleus. The location of the nucleus was defined to be the location of the peak of the continuum light from the galaxy. It was determined for each spectrum by fitting a Gaussian to the continuum emission from the galaxy. The spectra are arranged so that distance increases from east to west. Column (2) gives the flux-weighted mean "relative velocity," and column (3) gives the error in the mean (see § III). We define the "relative velocity" as the velocity of the emission-line gas at a given pixel location minus the velocity of the emission-line



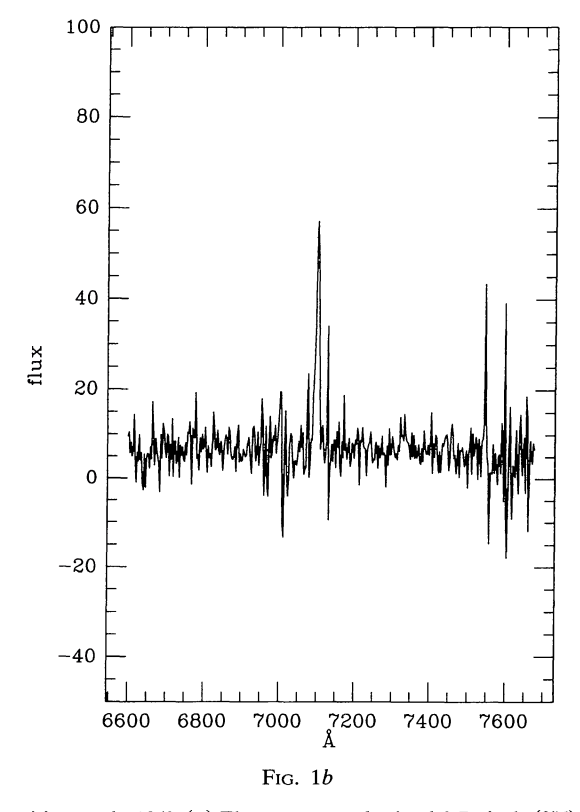


Fig. 1.—Typical spectrum, observed in PKS 0634-206, with the slit oriented in position angle 124°. (a) The spectrum obtained 0.7 pixels (0.6) west of the nucleus; (b) the spectrum obtained 10.7 pixels (9.72) west of the nucleus. Horizontal scale is in angstroms; vertical scale is in ADU.

TABLE 2 3C 29 Position Angle 12

х	Relative Velocity	Error	Velocity Width	Error	[O I]	[N II]	Нα	[N II]	[S 11]
0	0	20	218	13		197	169	660	
-1	+32	52	152	7			169	298	
+1	- 24	33	223	8			196	537	
+2		60	99	30			130	139	

TABLE 3
3C 33: Position Angle 19

x	Relative Velocity	Error	Velocity Width	Error	[O I]	[N II]	Нα	[N II]	[S 11]
-0.5	-27	12	540	5	2087	2115	10834	5400	5415
-1.5	-86	1	465			1436	2890	8442	
-2.5	-104	1	352	3	507	403	2369	1151	1476
−3.5	-88		548			152	1117	460	
−4.5	-77		294			92	532	222	
-5.5	-106		252				179		
+0.5	+24	8	504	18	2726	1852	9043	6322	7204
+ 1.5	+81	6	482	16	2376	2522	10497	5610	6104
+2.5	+1129	9	472	17	1315	1776	7622	3786	4208
+3.5	+ 192	7	397	22	445	1009	4157	1670	1752
+4.5	+213	7	232	25	155		763	439	688
+5.5	+214	8	218	31			351		185
+6.5	+204	•••	139	•••	•••	•••	92	•••	•••

TABLE 4
3C 63: Position Angle 90

x	Relative Velocity	Error	Velocity Width	Error	[O I]	[N II]	Ηα	[N 11]	[S 11]
-0.8	+10	21	571	22	397		1430	339	
−1.8	+26		572				550		
− 2.8	+40		640				322		
−3.8	+134		587				470	195	
−4.8	+84		633				447		
-5.8	+189		508				145		
+ 0.2	0		581				2068		
+ 1.2	0	99	577	74			845	164	
+ 2.2	+ 165		594				276		
+ 3.2	+254		354				68		
+ 4.2	+282		573				108		
+8.2	+16						131		
+ 9.2	−72	51					417	138	
+ 10.2	-10	•••	•••	•••	•••		292		•••

TABLE 5
3C 78: Position Angle 60

[S 11]	[N II]	Нα	[N II]	[1 O]	Error	Velocity Width	Error	Relative Velocity	x
2526	7875	2581	1821		36	529	2	-8	-0.8
	3067	374	946			528	2	+1	−1.8
	814					508		+ 77	-2.8
3995	10526	3272	2492		36	538	5	-6	+0.2
	5313	908	1617			513	1	-13	+1.2
	1565	108	701			552	6	-13	+ 2.2
	501					440		- 46	+3.2
	179					295		+53	+4.2

TABLE 6
3C 78: Position Angle 120

x	Relative Velocity	Error	Velocity Width	Error	[O I]	[N II]	Нα	[N II]	[S 11]
-0.4	-3	2	528	60	1154	2602	1979	8702	1825
- 1.4	+9	3	424	85		674	293	4203	
−2.4	+31		534					1638	
-3.4	+27		456					425	
+0.6	+4	7	524	18	636	2247	1521	8054	2290
+1.6	-6	5	463			556		2808	
+ 2.6	+3		626					1168	
+3.6	-27		463					395	
+4.6	+37		391					187	

TABLE 7
3C 78: Position Angle 180

x	Relative Velocity	Error	Velocity Width	Error	[O I]	[N II]	Ηα	[N II]	[S 11]
- 0.75 · · ·	+12		510			1934	1091	6295	•••
−1.75	+11		515					1844	
-2.75	+43		607					650	
-3.75	+30		231					119	
+0.25	+11	3	497	13		2223	1612	7657	2789
+1.25	-1		460			1182	702	4518	
+ 2.25	+2		412					1175	
+ 3.25	-2		576					463	

TABLE 8
3C 88: Position Angle 30

x	Relative Velocity	Error	Velocity Width	Error	[1 O]	[N II]	Ηα	[N 11]	[S 11]
-0.3	+6	10	431	34	702	1362	1405	3431	1794
−1.3	+28	20	265	115	479	874	848	2231	1334
−2.3	-1	19	299	55	196	362	433	999	499
−3.3	+8	29	209	73		93	107	460	383
−4.3	-5	20	254	50		87	118	326	
−5.3	+42		202					158	
-6.3	+42		396					170	
+0.7	+6	10	435	48	571	1250	1572	3215	2036
+ 1.7	-8	18	395	78		702	765	1807	978
+ 2.7	-14		369					564	
+ 3.7	+37		302					204	
+ 4.7	+ 103	•••	316					111	

TABLE 9
3C 88: Position Angle 90

x	Relative Velocity	Error	Velocity Width	Error	[O I]	[N II]	Ηα	[N II]	[S 11]
-0.4	+6	10	379	59	297	1292	1431	3046	1415
−1.4	+4	14	361	40	403	765	832	1979	1225
−2.4	-4	24	257	27	121	255	303	999	702
-3.4	+14	47	259	76	153	156	219	608	414
-4.4	-11	33	202	36		153	191	379	348
−5.4	-15		241					212	
−6.4	+25		403					138	
+0.6	+18	10	367	77		880	987	2556	1436
+ 1.6	+30	14	313	22		330	261	1298	1021
+ 2.6	+8	12	279	107		104	85	601	
+3.6	+2	59	301	3		140		282	
+4.6	-10		342					181	

TABLE 10 3C 88: Position Angle 150

x	Relative Velocity	Error	Velocity Width	Error	[I O]	[N II]	Нα	[N II]	[S 11]
-0.1	-4	7	490	63	913	1691	1963	4100	2966
- 1.1	-13	10	439	52	599	1171	1304	3115	2244
−2.1	-18	12	367	33	213	624	667	1808	1017
-3.1	+19	38	355	76	261	161	121	749	325
−5.1	-41		349					195	
+0.9	+37	10	404	69		1082	1371	3004	1464
+ 1.9	+11	14	362	104		522	463	1538	543
+ 2.9	+7	5	296			113	127	543	
+ 3.9	-16	•••	293	•••		•••	•••	259	, •••

TABLE 11 3C 98: Position Angle 163

x	Relative Velocity	Error	Velocity Width	Error	[1 O]	[N II]	Ηα	[N II]	[S 11]
-0.2	0	4	236	9	602	1491	5524	3440	2959
-1.2	+7	5	247	15	324	701	2612	1851	1477
-2.2	+ 21	11	243	21		233	806	632	690
−3.2	+ 20		302			131	170	380	
−9.2			291				106		
- 10.2	+ 192	11	198	58			198	77	
- 11.2	+ 197	1	242	20			330	52	
- 12.2	+210	4	284	5			254	95	
-13.2	+233	4	285	60			163	61	
-14.2	+ 180		207				42		
-31.8	-7		282				37	30	
+0.8	+3	5	223	18	387	925	3465	2335	2125
+1.8	+8	5	248	31		373	1382	919	1070
+2.8	+ 11	33	258	29		124	456	470	546
+3.8	-63		301			109	364	270	
+4.8	-55		255			71	193	134	
+5.8	-48		266				54		
+ 14.8	-34		263				69		
+ 15.8	-72		284				69		
+ 16.8	- 74		281				109		

TABLE 12
3C 98: Position Angle 163, 2".5 West

x	Relative Velocity	Error	Velocity Width	Error	[O 1]	[N II]	Ηα	[N II]	[S 11]
-0.2	-2	15	250	18		73	206	210	
−1.2	-28		322			162	260	293	
-2.2	-42	1	381	87			155	245	
−3.2	+17		92					62	
− 12.2	+281		277				95		
−13.2	+280	38	248	65			128	71	
−14.2	+ 299	3	224	9			88	40	
+0.8	-28	4	278	99			111	161	
+ 2.8	+4		524					165	
+ 15.8	-44		303				85		
+ 16.8	-186		288				79		

TABLE 13
3C 98: Position Angle 163, 2"5 East

x	Relative Velocity	Error	Velocity Width	Error	[O I]	[N II]	Ηα	[N II]	[S 11]
-0.2	+52	14	223	9		224	575	465	647
-1.2	+29		252			214	228	349	
-2.2	+30		244					101	
-8.2	+ 156		297				88		
−9.2	+140		386				137		
- 10.2	+ 155		218				155		
-11.2	+ 150		186				186		
- 12.2	+130		270				159		
- 13.2	+126		299				112		
+0.8	+38	13	201	15		306	1138	678	841
+ 1.8	+21	16	241	14		216	542	487	575
+ 2.8	-44		330			85	233	215	
+3.8	-119		413			168	244	289	
+4.8	-162		294			130	237	275	
+ 10.8	+92		< 60				60		
+ 11.8	+87	22	143	15			115	40	
+ 12.8	+129		157				72		
+ 13.8	+34		370				75		
+ 14.8	+ 18		240				66		

TABLE 14
3C 98: Position Angle 163, 5" East

x	Relative Velocity	Error	Velocity Width	Error	[1 O]	[N 11]	Нα	[N II]	[S 11]
- 10.2	+ 148		195				38		
-11.2	+ 132		129				69		
- 12.2	+85		149				76		
-13.2	+85		155				67		

TABLE 15
PKS 0634–206: Position Angle 85

x	Relative Velocity	Error	Velocity Width	Error	[O I]	[N п]	Ηα	[N II]	[S 11]
-0.9	-53	6	334	1	487	1704	9530	3157	2286
-1.9	-117	7	287	4	228	680	4175	1672	1362
-2.9	-140	35	237	10	134	439	2121	891	600
-3.9	-156	35	251	12		297	1415	534	831
-4.9	-133	7	195	34			393		
-5.9	-106		77				215		
-6.9	-108		< 60				134		
-7.9	-113		88				76		
-8.9	-134		< 60				97		
- 9.9	-134		< 60				69		
− 10.9	-62		108				108		
+0.1	+23	8	378	2	575	1847	9988	3729	2720
+1.1	+97	6	364	6	409	1455	7642	2736	2047
+ 2.1	+ 183	9	276	11	165	689	3843	1241	1113
+3.1	+215	8	211	18	131	624	1591	624	395
+4.1	+224	11	224	26		232	784	421	248
+5.1	+ 225	32	262		•••		279	203	180
+6.1	+ 191	4	214				149	134	
+ 7.1	+211	27					91	96	73
+8.1	+ 103							80	
+9.1	+116	•••	•••	•••	•••	•••	•••	51	• • • •

TABLE 16
PKS 0634-206: Position Angle 124

x	Relative Velocity	Error	Velocity Width	Error	[O I]	[N 11]	Нα	[N II]	[S 11]
-0.3	- 25	6	397	9	519	1727	9353	3142	1926
- 1.3	-82	11	349	7		1113	6170	2242	1309
-2.3	-109	13	283	21		621	2953	1148	613
-3.3	-166		210	24			933	521	312
-4.3	-192		161	47			737	361	
−5.3	-201		103	27			624	223	
−6.3	-194		90	24			553	191	149
<i>−</i> 7.3	-180		74	13			306	82	
−8.3	-170		129	10			208	61	
- 9.3	– 79		200				121		
-10.3	+62		< 60				72		
−11.3	+34		120				61		
−12.3	-108		< 60				65		
−13.3	-149		120		• • •		81		
−14.3	-68		< 60				74		
+ 0.7	+3	8	395	8	328	365	7706	2673	1891
+ 1.7	+ 57	18	365	27		361	2168	1296	814
+ 2.7	+66	24	262	105	• • •	157	707	304	• • •
+ 3.7	+170	20	308	77	• • •	116	371	176	• • •
+ 4.7	+152	•••	235		• • •	• • •	239	•••	
+ 5.7	+186		216			• • •	326	• • •	
+ 6.7	+205		178		• • •		359		
+ 7.7	+226		170				401		
+ 8.7	+219		153	• • •		• • •	470	• • •	• • •
+ 9.7	+205		243			• • •	529	•••	
+ 10.7	+129	• • •	120	• • •		• • •	745	•••	• • •
+ 11.7	+222	•••	282	•••		•••	373	•••	
+ 12.7	+231	•••	173	42	• • • •		414	135	
+13.7	+250	• • • •	102	20	• • •	• • •	319	67	• • • •
+14.7	+259	•••	114	37	• • •		200	62	• • • •
+15.7	+221	•••	< 60	•••	• • •	• • •	94	53	•••

TABLE 17
PKS 0634–206: Position Angle 85, 21" North

x	Relative Velocity	Error	Velocity Width	Error	[O I]	[N II]	Нα	[N 11]	[S II]
-0.1	+ 28	20	191				226	31	
-1.1	-3		180				144		
-2.1	-8		154				165		
-3.1	+38		155				262		
-4.1	+ 56		120				306		
-5.1	+ 49		74				240		
-6.1	+32		113				189		
−7.1	-4		147				129	•••	
-8.1	-2		109				60		
+0.9	+ 47		96				310		
+1.9	+ 38		82				409		
+2.9	+ 28	• • •	98				388		
+3.9	+62	• • •	< 60				276		
+4.9	+ 70		96				301		
+5.9	+ 66	• • •	96				362		
+6.9	+ 70		114				401		• • • •
+7.9	+85	• • •	143				400		
+8.9	+101		148				308		
+9.9	+ 101		90				225		
+ 10.9	+89		144				169		
+ 11.9	+ 94		67				128		
+ 12.9	+111		104				105		
+ 13.9	+106		106				132		
+ 14.9	+115		66				147		
+ 15.9	+126		< 60				125		
+ 16.9	+120		< 60				94		
+ 17.9	+162	• • •	128				67		
+ 18.9	+210	•••	294	•••	•••	•••	74	•••	•••

TABLE 18 3C 192: Position Angle 0

x	Relative Velocity	Error	Velocity Width	Error	[O I]	[N II]	Нα	[N II]	[S 11]
-0.7	+ 52	3	311	0		200	721	527	497
− 1.7	+117	4	321				474	139	
-2.7	+ 201	10	310	7			70	63	
+0.3	+ 10	7	288	11	88	258	883	771	649
+1.3	-42	26	304			148	525	269	
+2.3	-8	51	297	92			67	63	
+3.3	-71		359	0			54		

TABLE 19 3C 192: Position Angle 145

x	Relative Velocity	Error	Velocity Width	Error	[I O]	[N II]	Нα	[N II]	[S 11]
-0.1	-13	1	274	5		1167	4196	3624	3505
-1.1	-45	4	285	0		586	2311	1563	1589
−2.1	- 74	19	306	20		160	610	343	393
−3.1	-221	42	212	72			213	92	
−4.1	-186		168				153		
-5.1	-217		168				115		
−6.1	-231		62				92		
-7.1	-231		106				85		
-8.1	-236		81				105		
−9.1	-225		86				100		
- 10.1	-224		< 60				37		
- 20.1	-182		< 60				61		
-21.1	-193		101				73		
− 22.1	-230		135				98		
−23.1	-207		95				68		
+0.9	+16	1	272	8		728	2797	2251	2198
+1.9	+100	7	267	5		259	2110	683	756
+2.9	+114	6	187	39		30	277	152	172
+3.9	+ 107	• • •	205				112		

TABLE 20 3C 192: Position angle 0, 4" East

x	Relative Velocity	Error	Velocity Width	Error	[I O]	[N II]	Ηα	[N II]	[S 11]
+1.3	-217		< 60				50		
+2.3	-191		< 60				84	22	
+3.3	-190		97				108		
+4.3	-181		200				116		
+5.3	-227		65				62		
+6.3	-219		143				97		
+7.3	-238		< 60				126		
+8.3	-240		88				111		
+9.3	-274		171				33		

TABLE 21
3C 192: Position Angle 15, 10...5 West

x	Relative Velocity	Error	Velocity Width	Error	[I O]	[N II]	Нα	[N II]	[S 11]
-0.5	+313		224				144		
-1.5	+338		200				120		
-2.5	+222		399				116		
-3.5	+196		386				181		
-4.5	+65		508				163		
−5.5	-126	28	415	69		25	197	117	111
-6.5	-211	13	342	33			153	93	
-7.5	-283		248				68		
+0.5	+287	11	97	20			162	49	
+1.5	+280	13	149	33			162	95	134
+2.5	+323	12	352	55			208	95	
+3.5	+272	14	171	26			69	67	

TABLE 22 3C 196.1: Position Angle 52

x	Relative Velocity	Error	Velocity Width	Error	[1 O]	[N II]	Нα	[N II]	[S 11]
-1.8	-8		431					392	
-2.8	-60	31	333	50			157	331	
-3.8	-36		328				285	780	
-4.8	+8							145	
+0.2	0		422				372	798	
+1.2	-67		513					386	
+ 2.2	+ 75		133					87	

TABLE 23 3C 227: Position Angle 38

x	Relative Velocity	Error	Velocity Width	Error	[O I]	[N 11]	Нα	[N II]	[S 11]
-0.6	-17		475				4527		
-1.6	-17		386				1939		
-2.6	+5		351				686		
-3.6	-19		245				211		
-4.6	-42		338				129		
-5.6	-25		569				214		
-6.6	-20		105				137		
-7.6	+100		< 60				45		
-15.6	+ 43		161				48		
-18.6	+116		235				78		
-21.6	-27		264				118		
-24.6	-54		267				78		
-27.6	-148		275				115		
-30.6	-130		247				139		
−33.6	-115		314				206		
-36.6	-150		270				78		
-39.6	-285		342				60		
+0.4	0		444				4744		
+1.4	- 16		350				1941		
+ 2.4	- 13		487				991		
+3.4	-64		513				337		
+4.4	-61		517				150		
+ 5.4	-150		323				77		
+ 9.4	+60		433				107		
+ 12.4	+ 17		284				141		
+ 15.4	+ 94		182				140		
+18.4	+71		275				131		
+21.4	+ 70		340				114		
+24.4	+62		205				56		
+33.4	+251		< 60				41		•••
+36.4	+ 72		112				40		
+39.4	+114		< 60				26		

TABLE 24 3C 227: Position Angle 121

x	Relative Velocity	Error	Velocity Width	Error	[O I]	[N 11]	Ηα	[N II]	[S 11]
-0.1	0		496			496	4464	1553	···
-2.1	+20		417			380	1828	550	·
-3.1	+17	8	343	13			895	153	
−4.1	+85		351				495	120	
−5.1	+117		365				430	78	
−6.1	+ 101		388				468	140	
− 7.1	+ 108		341				509	157	
-8.1	+86		227				405	100	
−9.1	+73	2	233				450	120	
-10.1	+ 54		233				466	165	
-11.1	+71	5	199	20			363		
−12.1	+62		216				310		
−13.1	+100		260				194		
−14.1	+ 129		209				152		
− 15.1	+ 205		204				87		
+0.9	-5	1	434			382	3154	592	
+ 1.9	-18	1	444			263	1914	578	
+ 2.9	-30	1	454			96	1048	151	
+ 3.9	-10		374				462		
+ 5.9	+10		383				323		
+6.9	-17		197				173		
+ 7.9	-40		355				147		
+8.9	-42		127				92		
+ 9.9	-71		178				106		
+ 10.9	-67		305				228		
+ 11.9	-101	•••	129	•••			227		
+ 12.9	-89		155				210		
+ 13.9	-97		147				225		
+ 14.9	-113		73				122		
+ 15.9	-105		135		• • •	• • •	138		

TABLE 25
3C 227: Position Angle 121, 5".2 South

x	Relative Velocity	Error	Velocity Width	Error	[O I]	[N II]	Нα	[N II]	[S 11]
-0.1	- 38		360				95		•••
- 1.1	+13		369				134		
−2.1	+ 77		287				103		
−2.6	+ 16		167				133		
−4.6	+87		204				70		
−6.6	+119	4	229	9			148	32	
−10.6	+114	12	280	31			354	86	
−12.6	+118	18	231	5			211	74	
−14.6	+121		216				131		
+ 0.9	- 59		396				124		
+ 1.9	-49		420				150		
+ 2.9	-116		152				85		
+ 3.9	-50		341				116		
+ 5.9	+4		414				93		
+ 7.4	+36		359				64		
+ 9.4	-38	4	394	165			103	20	
+11.4	-143		144				150		
+13.4	-166	11	226	26			209	50	
+ 15.4	-113		262				145		
+17.4	-118	46	160	20			67	32	
+ 19.4	-71		269				32		
+ 21.4	-83		189	•••	•••		55		•••

TABLE 26
3C 227: Position Angle 172, 27" East

x	Relative Velocity	Error	Velocity Width	Error	[O I]	[N II]	Ηα	[N II]	[S 11]
-1	+ 157		477				48		
-6	+237		498				42		
-11	+303		209				38		
−16	+150		249				23		
+4	+113		443				38		
+9	+27		138				16		

TABLE 27 3C 264: Position Angle 85

x	Relative Velocity	Error	Velocity Width	Error	[1 O]	[N 11]	Нα	[N II]	[S 11]
-1.0	-4	15	453	50		652	998	2186	
- 2.0	-1		603					903	
0.0	0	9	461	9		1689	2555	4874	
+1.0	+17	6	339			713	892	2068	
+2.0	+6		337	•••	•••			418	

TABLE 28 3C 264: Position Angle 175

x	Relative Velocity	Error	Velocity Width	Error	[I O]	[N 11]	Нα	[N II]	[S 11]
- 1.0	0	17	372			1157	1497	3963	
-2.0	-2	32	350			670	481	1426	
-3.0	+25		387					616	
0.0	00	10	340			1540	2263	5376	
+ 1.0	-12	15	348			1547	1886	4640	
+ 2.0	-31	20	329			832	768	2261	
+3.0	-6		236					1012	

TABLE 29 3C 272.1: Position Angle 85

x	Relative Velocity	Error	Velocity Width	Error	[1 O]	[N 11]	Нα	[N 11]	[S 11]
-1.0	-73	4	362	6		5673	6870	18011	14145
-2.0	-103	8	292	13		3649	4093	10532	8780
-3.0	-103	7	256	24		2529	2623	7661	3972
-4.0	-102	10	177	27		1453	1439	4253	2527
-5.0	-114	7	157	13		1216	1324	3828	3190
-6.0	-135	4	150	16		1052	1204	3331	2579
-7.0	-151	5	135	12		893	1120	2980	1791
-8.0	-161	4	150	12		822	920	2352	1778
-9.0	-180	7	145	32		312	445	1241	1171
− 10.0	-167		182					718	
0.0	-9	10	417	12		5592	7120	21757	22366
+1.0	+62	11	355	5		4732	6173	17369	13041
+2.0	+81	6	248	22		2548	3576	9382	6708
+3.0	+85	8	166	17		1340	1584	4545	2672
+4.0	+85	14	164	17		551	640	2708	1193
+5.0	+89		176			• • •		1223	
+6.0	+ 101		362					930	
+7.0	+57		426					777	
+8.0	+89							750	
+9.0	+ 79		228					546	
+ 10.0	+ 79		311					546	
+ 11.0	+47		183					560	
+ 12.0	+79							471	

TABLE 30 3C 272.1: Position Angle 175

x	Relative Velocity	Error	Velocity Width	Error	[O I]	[N II]	Ηα	[N II]	[S 11]
-0.8	+50	8	344	34		1632	2113	8111	4811
-1.8	+63	11	298	12		1193	1399	5058	3168
-2.8	+ 57	20	297	21		699	373	2498	2095
+0.2	+25	15	489	23		4394	5456	13134	12634
+1.2	-5	6	403	10		3025	3189	8523	6223
+ 2.2	-8	7	258	28				3636	3802
+ 3.2	-1		332					1715	
+4.2	-71		511					977	

TABLE 31 3C 285: Position Angle 95

x	Relative Velocity	Error	Velocity Width	Error	[O I]	[N II]	Ηα	[N II]	[S 11]
0	+ 25	26	472	16		507	3618	1283	
-1	0	9	415	16	242	692	3647	1077	
-2	+ 39	10	369	70	301		1051	56	
-3	+ 145	2.	197	27			814	380	
-4	+217	6	208	20			1392	481	445
-5	+226	8	190	11	120		1181	393	347
-6	+239	23	156	8	74		531	190	
+1	+63	7	387	22		475	2251	784	
+2	+ 23	9	216	51	205	221	1457	555	705
+3	-6	3	166	33	199	421	2740	711	978
+4	-42	4	113	18	216	375	1966	644	519
+5	- 49	12	123	32	216	125	714	228	
+6	-68	10	94				326	101	
+7	-103		130				132		

TABLE 32 3C 285: Position angle 140

x	Relative Velocity	Error	Velocity Width	Error	[I O]	[N II]	Нα	[N II]	[S 11]
0	-36	33	432	11	206	362	2387	957	
-1	+112	11	409			380	1975	786	
-2	+ 161	13	222				544	234	
-3	+229	12	277				286	201	
-4	+250	7	213				579	119	
-6	+265		155				126		
+1	-96	21	371			390	1390	555	
+2	∽ 97	7	211			159	647	271	
+3	-108	10	147				719	145	
+4	-136	25	148			70	352	126	
+5	-45		< 60				93		
+6	-80		80				99		
+7	-107		262				100		
+8	-118		< 60				91		
+9	-130		97				92		
+10	-139		110				100		
+11	-121		96				103		

TABLE 33
PKS 1345+125: Position Angle 60

х	Relative Velocity	Error	Velocity Width	Error	[O I]	[N II]	Ηα	[N II]	[S 11]
-0.5	-2	52	562	42		722	885	1285	942
-1.5	+1		498				376		
-2.5	+52	40	378			264	344	455	
+0.5	+1	46	759	5	691				3025
+1.5	-1	26	644	23	1033				4005
+ 2.5	+60	29	575	0	477				1835
+3.5	+ 156	15	512	7		283	1102	925	975
+4.5	+171	37	531	11	•••	205	470	545	642

TABLE 34 3C 353: Position Angle 160

x	Relative Velocity	Error	Velocity Width	Error	[O I]	[N II]	Ηα	[N 11]	[S 11]
-1	+4	2	619	7	785	1340	2384	3306	2594
− 2	+94	19	402	78		296	466	809	402
−3	+107		295			43	148	192	
-4	+ 74	16	211			62	116	126	
0	0	8	655	31		1884	4143	4993	6006
+ 1	+65	13	601	32	687	1042	1999	2436	2912
+ 2	+112	18	356	18		251	412	460	497
+3	+48		359			173	108	437	

TABLE 35 3C 403: Position Angle 20

x	Relative Velocity	Error	Velocity Width	Error	[O I]	[N II]	Ηα	[N II]	[S 11]
0	+24	13	326	4	754	1594	4763	4509	2863
- 1	-40	8	319	6	526	1235	4149	3212	1839
- 2	-115	8	319	3	93	712	2100	1562	926
- 3	-202	15	228			302	810	790	
- 4	-218	8	255	32		258	485	511	
-5	-247	21	231	20			213	233	
-6	-167							200	
- 7	-192		167					130	
- 1	+80	11	352	19	617	1363	3912	3532	1983
- 2	+ 193		259	8	306	727	1710	1899	1210
- 3	+249	5	132	23	191	375	758	1250	716
- 4	+257	4	75	11	183	274	548	818	482
- 5	+252	5	122	27	179	112	270	395	341
- 6	+272	9	235			101	133	196	

TABLE 36 3C 403: Position Angle 110

x	Relative Velocity	Error	Velocity Width	Error	[I O]	[N II]	Ηα	[N II]	[S 11]
0	-16	9	375	14	768	1676	5687	4501	3011
– 1	37	10	402	20	572	1483	4369	3116	1928
-2	. – 78	17	399	13		546	1509	1126	
-3	-114	26	358				425	352	
+1	. +7	9	383	11	443	1561	4358	3371	1852
+2	+ 17	13	397			448	1063	978	

TABLE 37 3C 405: Position Angle 160

x	Relative Velocity	Error	Velocity Width	Error	[O I]	[N II]	Ηα	[N II]	[S 11]
0	-1	6	387	17	1119	2373	3698	6273	4159
- 1	-46	3	324	4	666	1114	1799	3158	2313
- 2	+2	9	361	29	237	301	448	945	590
- 3	+ 28	21	392	27		140	140	340	261
- 4	+100	6	378	22			106	113	
- 1	+60	4	401	8		2837	4466	7874	
- 2	+62	3	351	3	622	1942	3008	5569	3238
- 3	+49	5	340	19	208	608	979	1783	1129
- 4	+31	33	347	41				287	280

TABLE 38
3C 405: Position Angle 160, 2" West

x	Relative Velocity	Error	Velocity Width	Error	[O I]	[N II]	Ηα	[N II]	[S 11]
0	-106	6	329	21	358	556	912	1553	1057
-1	-81	8	322	18		366	583	1009	859
-2	-51	11	265	23		116	244	397	367
-3	+7	24	347	30		77	117	241	211
-4	+24	14	311	17		121	133	222	350
+1	– 99	10	454	3		565	859	1417	852
+2	-24	6	206	3		222	411	717	573
+3	+84	21	492	31		151	170	283	

TABLE 39
3C 405: Position Angle 160, 2" East

x	Relative Velocity	Error	Velocity Width	Error	[1 O]	[N II]	Ηα	[N II]	[S 11]
0	+67	2	338	12	716	1345	2304	3783	2462
- 1	+65	5	318	11	314	686	1083	1652	1098
-2	+90	9	305	40	158	141	615	917	302
+ 1	+98	16	355	10	876	1740	2919	4852	3489
+ 2	+130	3	331	11	688	1576	2385	4402	2952
+3	+131	3	314	16	400	832	1315	2522	1974
+4	+119	6	352	1		357	584	977	691
+5	+ 149	13	498	14			207	446	

TABLE 40 3C 433: Position Angle 129 A.

x	Relative Velocity	Error	Velocity Width	Error	[O I]	[N II]	Ηα	[N 11]	[S 11]
- 0.5	-14	6	500	19	1186	2379	5094	5785	4010
– 1.5	-71	7	470	17	671	1325	3098	3510	2492
−2.5	-120	8	413	37	447	942	2541	2738	2018
−3.5	-168	19	417	39	391	495	1811	2257	714
−4.5	-218	24	657			388	963	1263	
-5.5	-313	26	661			102	261	353	
+ 0.5	+16	12	488	42	1277	2209	4621	4809	2492
+ 1.5	+16	42	644	34	603		2426	2383	

TABLE 40—Continued B.

Offset	Relative Velocity	Total Flux
-0.5	0	13258
-1.5	-41	7933
-2.5	-91	6221
-3.5	-64	4563
−4.5	-132	2614
-5.5	-215	716
+0.5	0	11639
+1.5	+7	6712
+2.5	-360	6370
+3.5	-411	5226
+4.5	-187	3949
+5.5	-119	4185
+6.5	-91	2960
+7.5	+ 137	1445

Notes.—Key to part B is as follows: Col. (1): offset in pixels from location of nucleus; col. (2): relative velocity derived as the centroid of the $H\alpha + [N \text{ II}]$ complex; col. (3): total flux in that line complex.

TABLE 41 3C 442: Position Angle 36

x	Relative Velocity	Error	Velocity Width	Error	[ı O]	[N 11]	Нα	[N 11]	[S 11]
-0.6	-4	12	362		133	576	702	1861	•••
-1.6	-22	9	276	11	244	646	834	2129	1251
-2.6	-9	9	272			207	287	811	
-3.6	+6		358					152	
+0.4	+18	16	496	76		1670	2102	4397	1836
+1.4	-24	9	390			1127	1259	3294	
+2.4	-36	21	257	23		190	132	675	

TABLE 42 3C 442: Position Angle 126

x	Relative Velocity	Error	Velocity Width	Error	[O I]	[N II]	Нα	[N 11]	[S 11]
-0.6	+19	15	465	39		1627	1979	4600	2139
-1.6	-28		354					1155	
−2.6	-10		372					562	
-3.6	-24		107					205	
−4.6	69		281					382	
-5.6	-115		266					173	
+0.4	-14	7	455	43		2437	3002	6590	2894
+ 1.4	-17	7	285	27		717	809	2282	811
+ 2.4	0	8	261			381	310	1079	
+ 3.4	+55	16	193			171	146	515	
+4.4	+ 135		250					320	
+5.4	+67	•••	198	•••		•••	•••	109	

406 BAUM ET AL.

gas in the nucleus. We have calculated the velocity of the nuclear gas as the flux-weighted velocity of the gas detected within 1 pixel of the nominal position of the nucleus on all slit position angles obtained through the nucleus, with resulting typical errors on the mean of less than 10 km s⁻¹. Column (4) gives the flux-weighted mean (rest frame) velocity width of the lines (FWMH), and column (5) gives the error on the mean. Columns (6), (7), (8), (9), and (10) give, respectively, the fluxes (in ADU; the spectra are uncalibrated; see above) for the [O I] λ 6300.3, [N II] λ 6548.1, H α λ 6562.8, [N II] λ 6583.4, and [S II] λ 6716.4 plus λ 6730.8.

Results for each source are presented graphically, with one plot for each observed position angle. These figures are organized as follows. For each source we plot along the abscissa the distance along the slit, in units of kiloparsecs along the bottom axis and in units of arcseconds along the top axis. Here, and throughout, we assume a Hubble constant of 75 km s⁻¹ Mpc⁻¹. For spectra which pass through the nucleus, the distance given is the distance from the nucleus of the source. For spectra in which the slit was offset from the nucleus, the distance given is the distance along the slit from the projection of the nucleus onto the slit (see Fig. 2). The spectra are arranged so that distance increases from east to west.

Along the ordinate we plot the following. In (a), we plot the relative velocity. In (b), we plot the integrated flux of either the $H\alpha$ or the $[N\ II]\ \lambda6583$ line, as specified in the figure, either as a log-linear plot, or as a linear-linear plot, which should be self-evident from the figure. In (c), we plot the velocity width (Gaussian FWHM, corrected to the rest frame of the host galaxy) of the emission-line gas. The points shown at $60\ \text{km s}^{-1}$ represent upper limits. Lines narrower than this are effectively unresolved in our observations. Where measured, we plot in (d) the $H\alpha$ to $[N\ II]\ \lambda6583$ flux ratio along the ordinate. As described above, the velocity and velocity widths of the emission-line gas were calculated

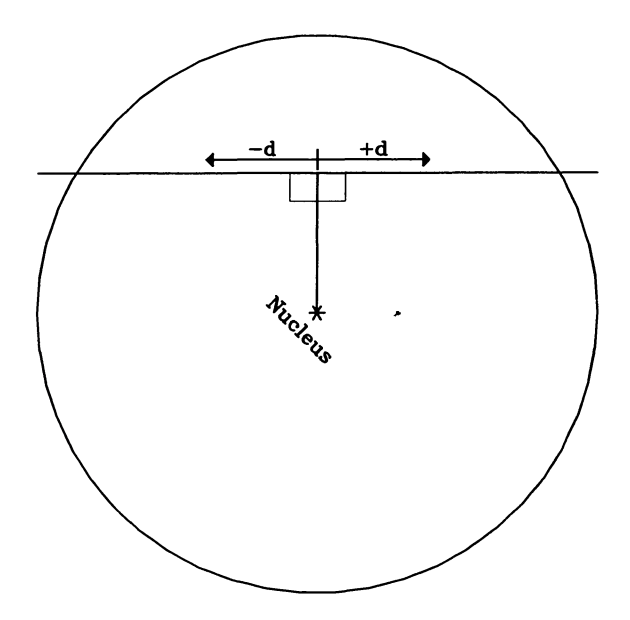


Fig. 2.—The geometry used to define distance along the slit in Figs. 3–43.

as the flux-weighted average of the centroids and widths, respectively, of all measured (narrow) emission lines at a given pixel location. These graphs are shown in Figures 3-43.

For the sources in which the emission-line nebula is complex and extended over many resolution elements, we also present contour maps of the emission-line nebula with overlays showing the velocity structure in the gas. These are presented in Figures 44–49. In these figures we show contours of the line emission (as taken from Paper I), with superposed circles whose size and shadings indicate, in Figures 44a-49a, the relative velocity of the gas, and in Figures 44b-49b, the FWHM velocity width of the measured lines. Velocity circles are drawn only every two or three pixels. The symbols used are the same in all six figures, and the key for the symbols can be found in Table 43.

The statistical properties of the sample and the interpretation of the results will be discussed in detail in a forthcoming paper (Paper II). Here we discuss the individual source properties. In the text we speak of the rotation velocity of the gas, which we define to be $v_{\rm rot} = \frac{1}{2}(v_{\rm plus} - v_{\rm minus})$, where $v_{\rm plus}$ is the velocity at which the rotation curve flattens on the side of the source showing positive velocities relative to the nucleus, and $v_{\rm minus}$ is the velocity at which the rotation curve flattens on the opposite side of the source.

In Paper I, we present narrow-band optical images of the emission-line nebulae, VLA images of the radio emission, and broad-band optical images of the optical host galaxies for each source. In addition, we describe the morphological properties of the individual sources and provide brief descriptions of, and references to, work done by other investigators. The reader may find the images and information presented in Paper I useful when reading the present paper.

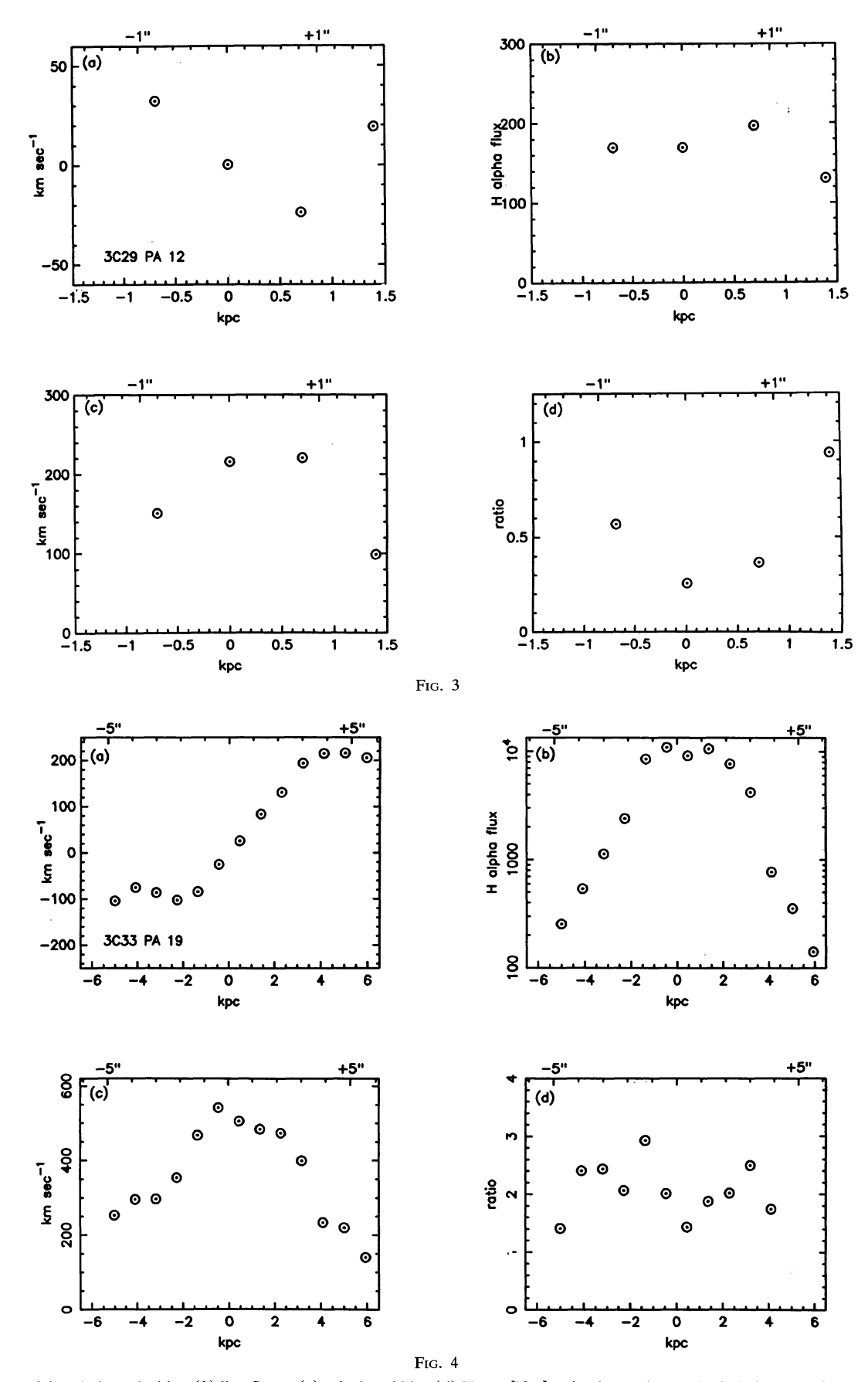
V. INDIVIDUAL SOURCE DESCRIPTIONS

a) 3C 29

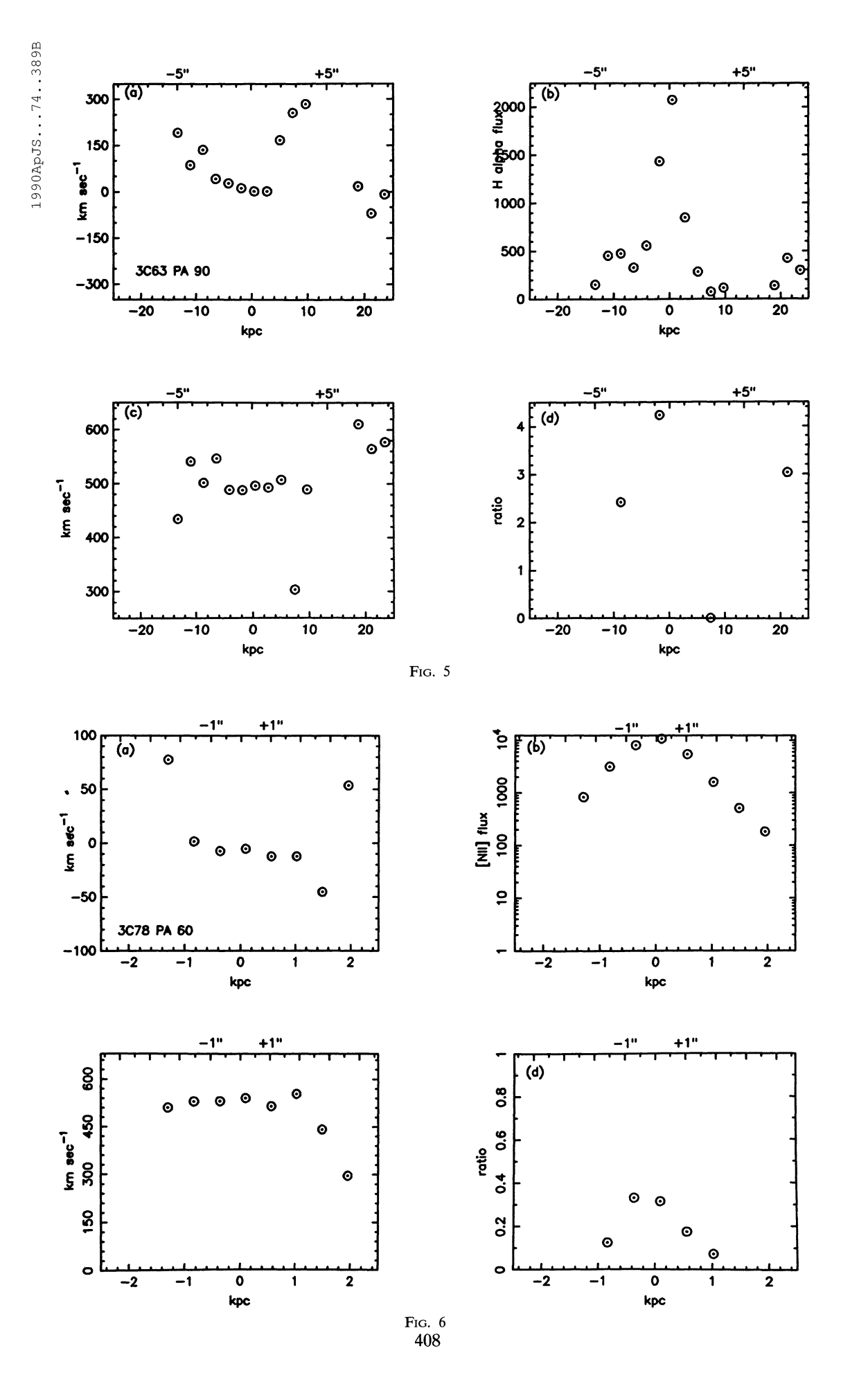
The narrow-band images presented in Paper I show nuclear line emission with a possible tail of emission-line gas extending to the north. Unfortunately, our long-slit spectra of this source were obtained under poor weather conditions, and we are unable to confirm (or dispute) the reality of this feature. The nuclear emission lines are quite narrow ($\sim 200~\rm km~s^{-1}$ FWHM).

b) 3C 33

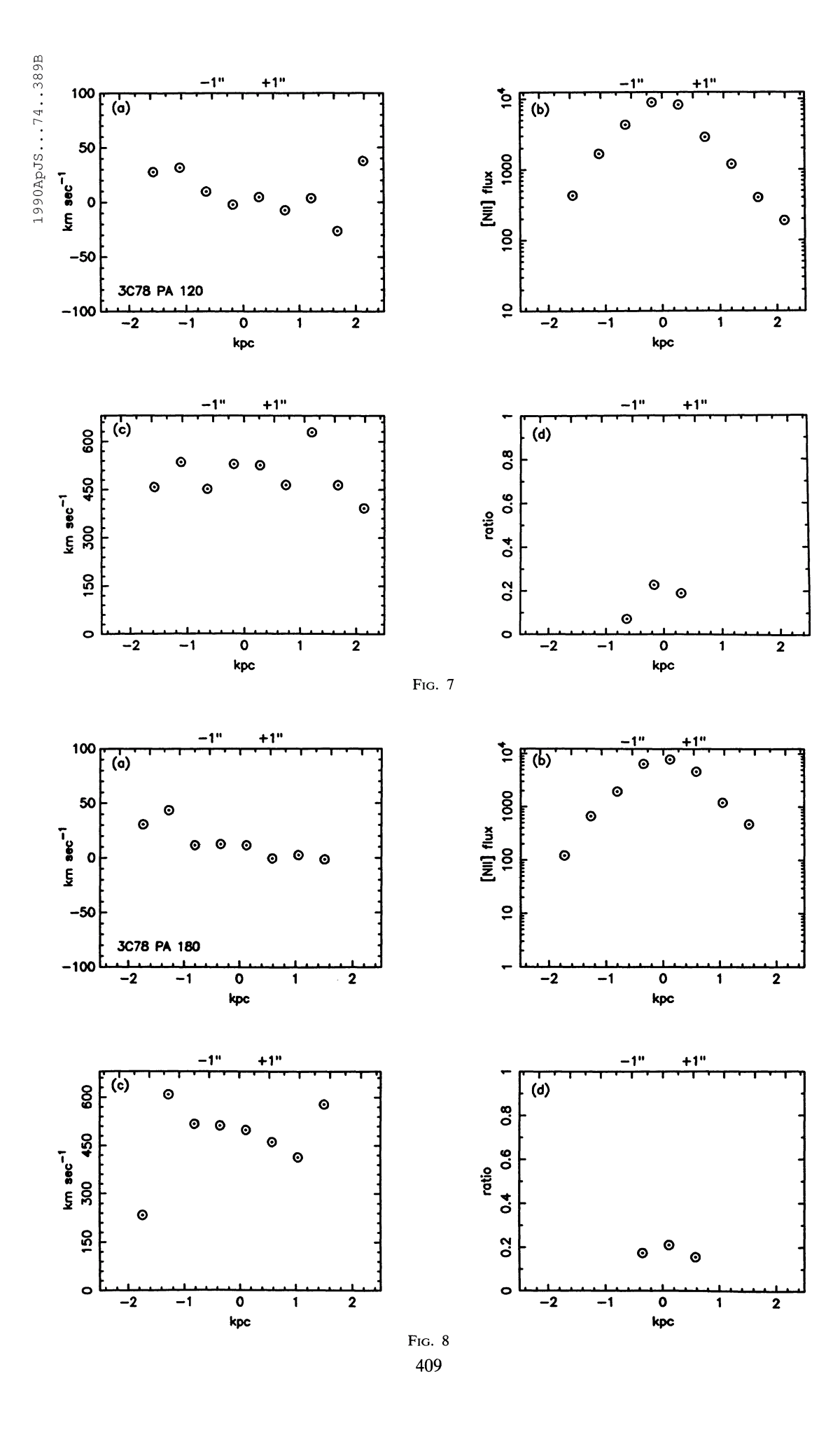
Previous long-slit spectroscopy of the disklike emission-line region in the inner parts of 3C 33 led Simkin (1977) and Heckman *et al.* (1985) to conclude that the line-emitting gas is rotating, with a rotation axis in a position angle of $\sim 19^{\circ}$ along the radio source axis, but askew to the minor axis of the gas distribution. We placed our slit along position angle 19° and find that the gas still shows a characteristic rotation pattern. We measure a rotational velocity of ~ 160 km s⁻¹, or roughly half of the maximum rotational velocity (detected along PA 110; Simkin 1977). We further find that the rotation curve in PA 19 is not symmetric about the nucleus of the galaxy, but that the center of the rotating disk is offset by ~ 1 kpc (1") from the galaxy nucleus, corresponding to a



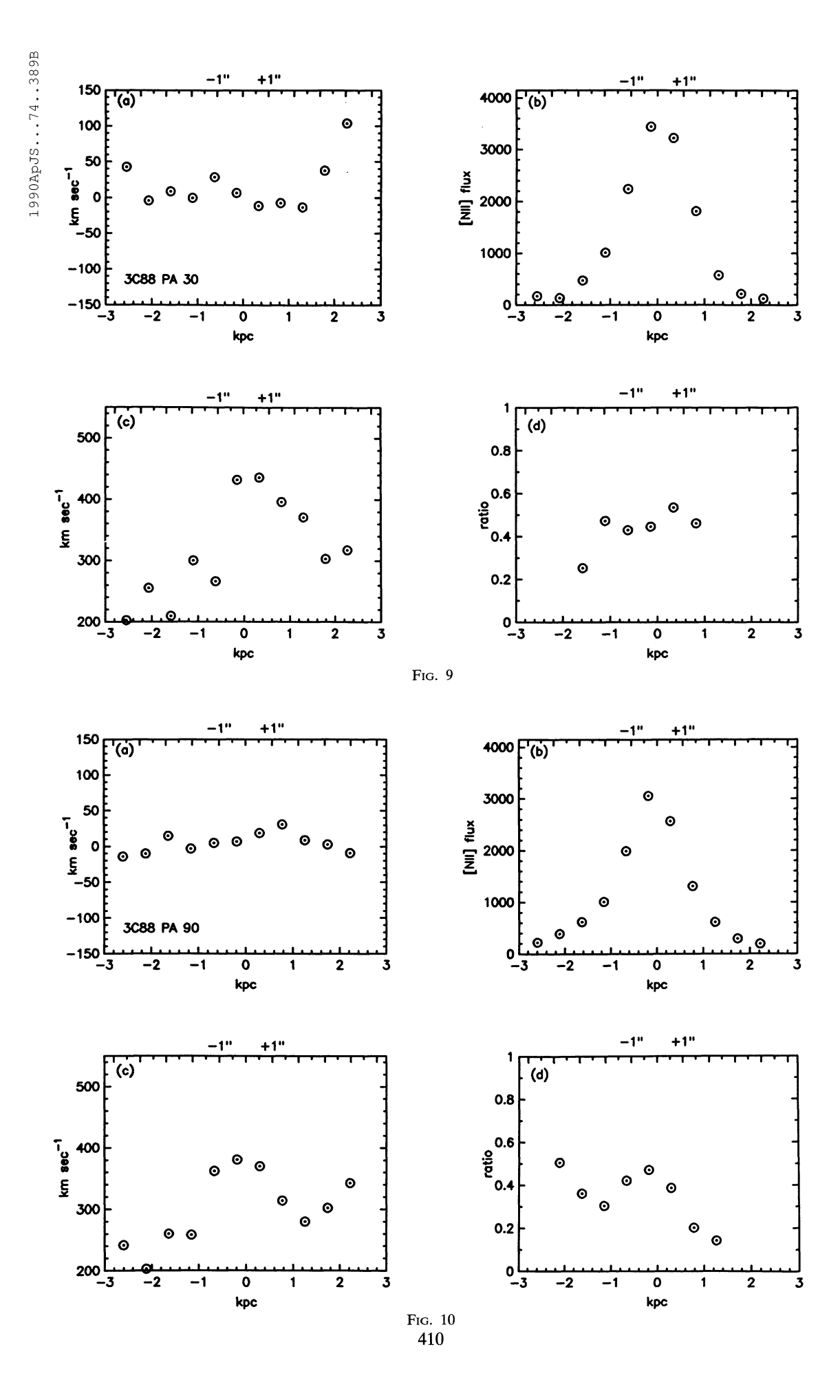
Figs. 3-43.—(a) Relative velocities, (b) line fluxes, (c) velocity widths, (d) $H\alpha$ to [N II] ratio observed at each pixel. See § IV for a more detailed description of the organization of these plots.



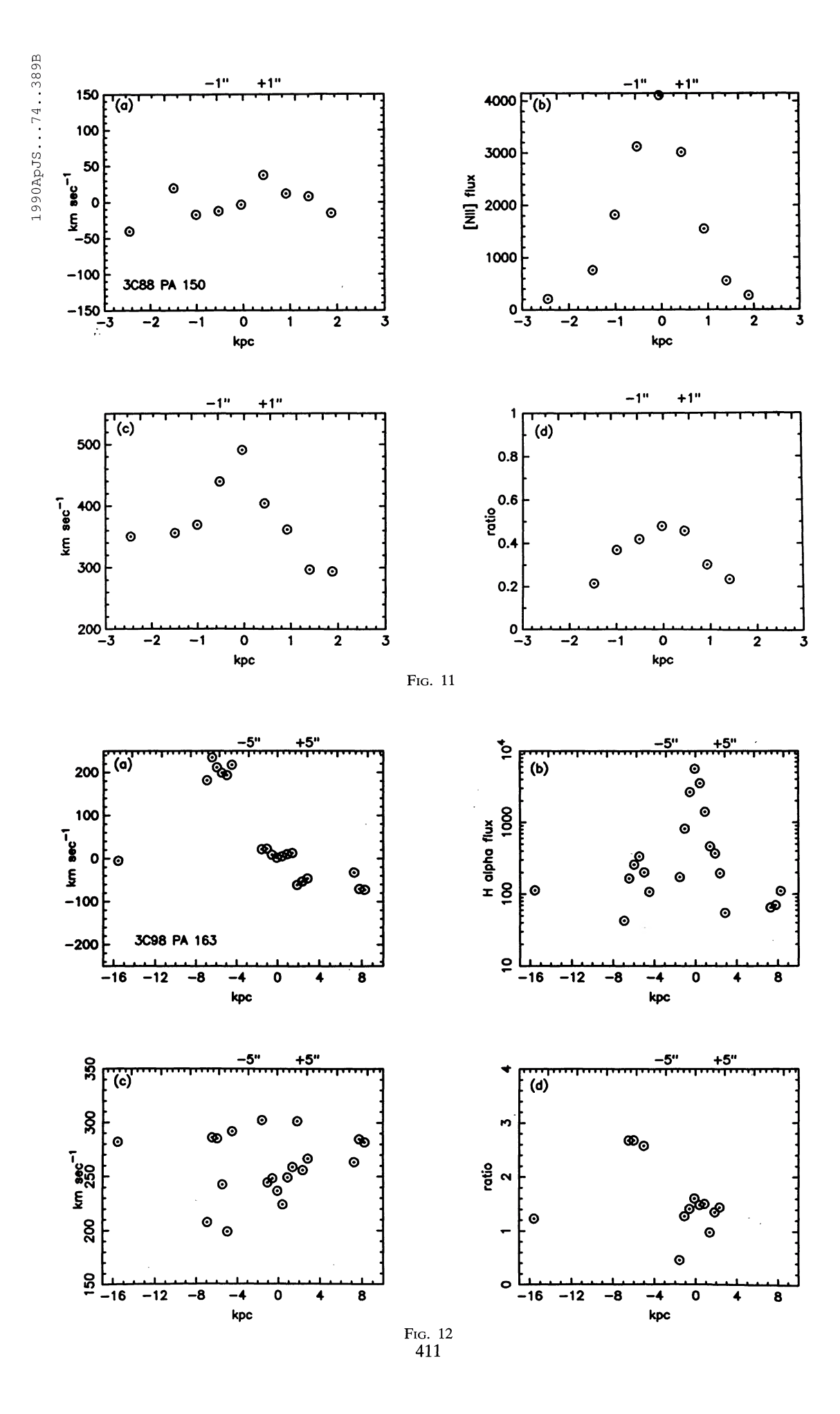
 $@ \ American \ Astronomical \ Society \ \bullet \ Provided \ by \ the \ NASA \ Astrophysics \ Data \ System$



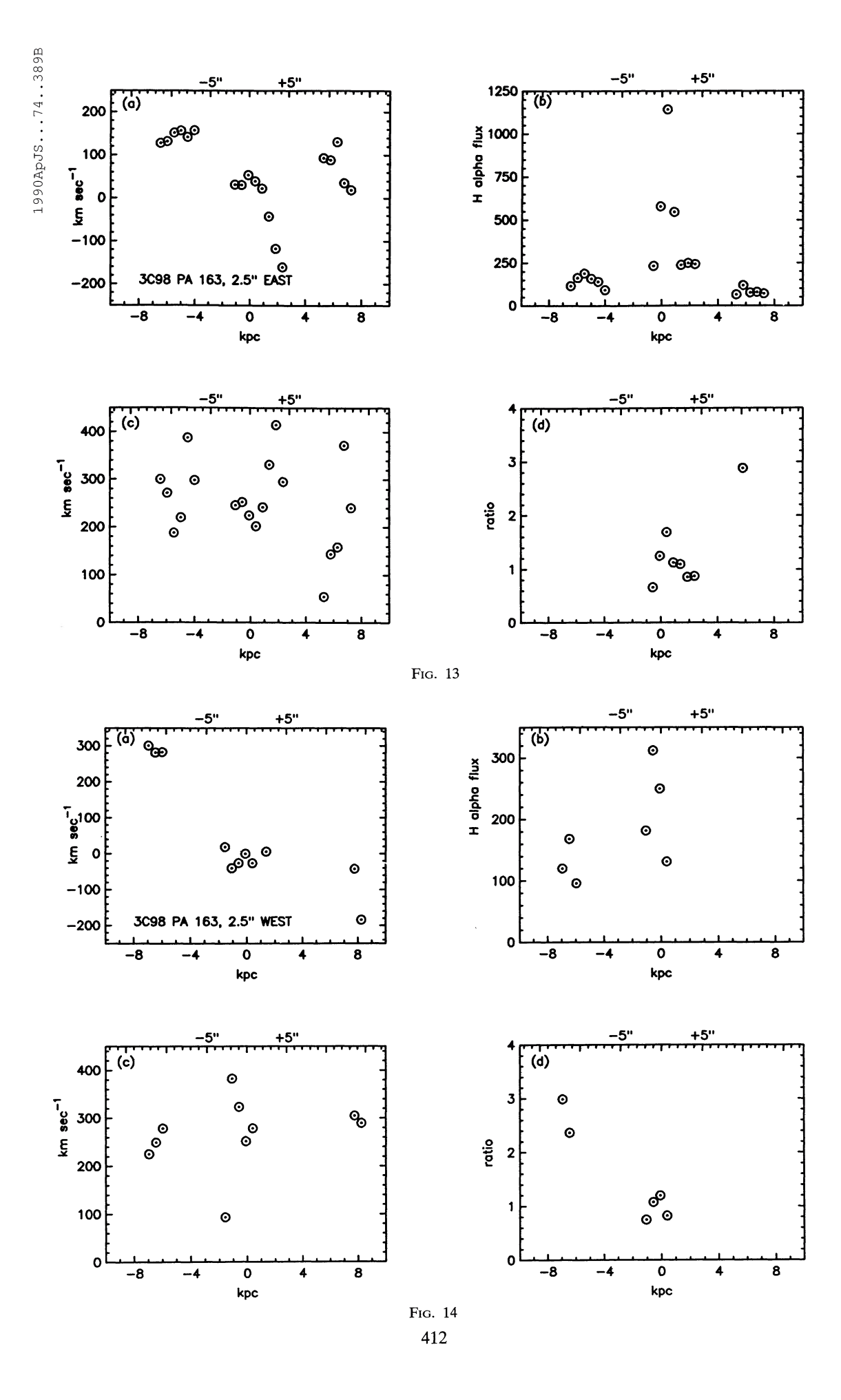
 $@ \ American \ Astronomical \ Society \ \bullet \ Provided \ by \ the \ NASA \ Astrophysics \ Data \ System$



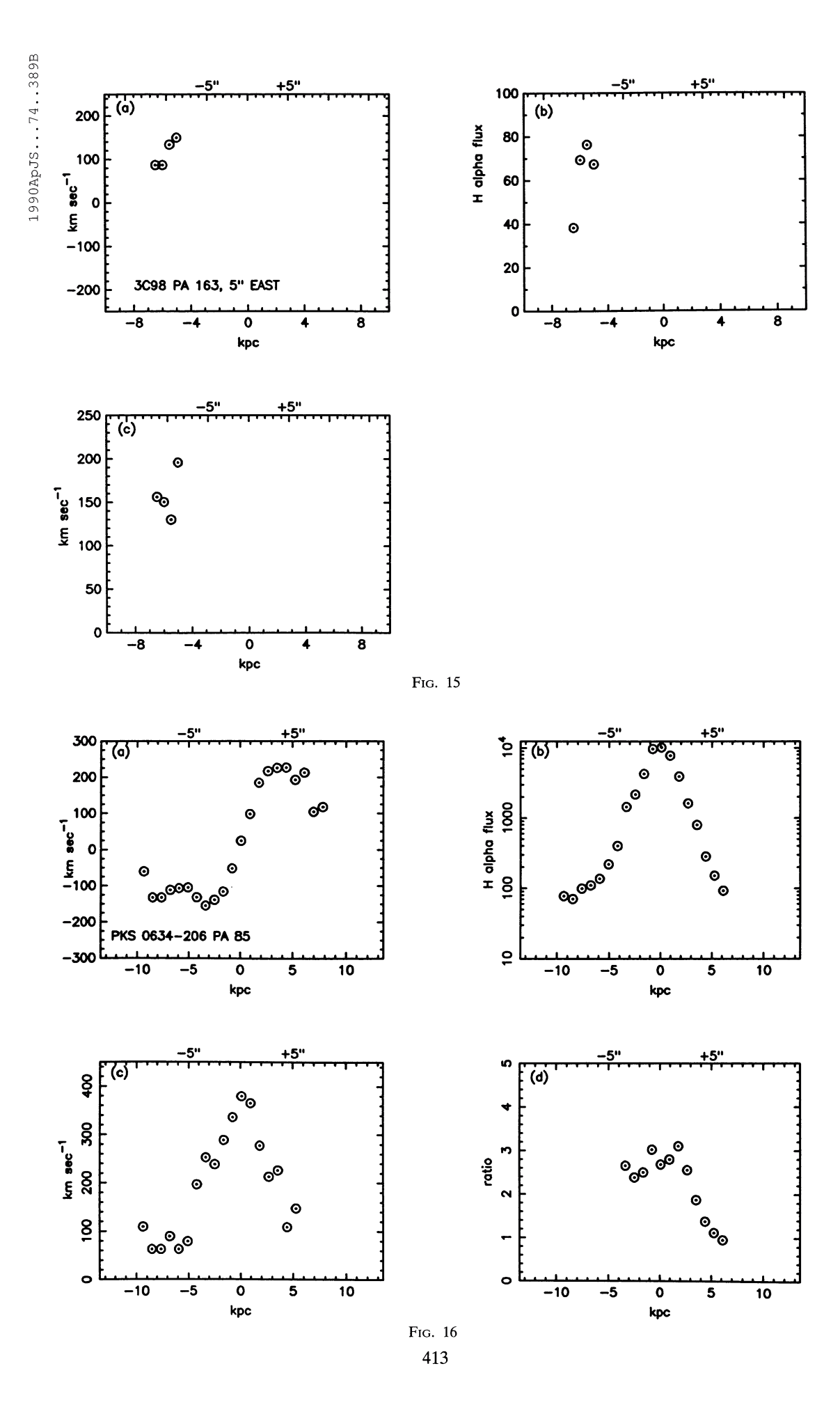
 \odot American Astronomical Society • Provided by the NASA Astrophysics Data System



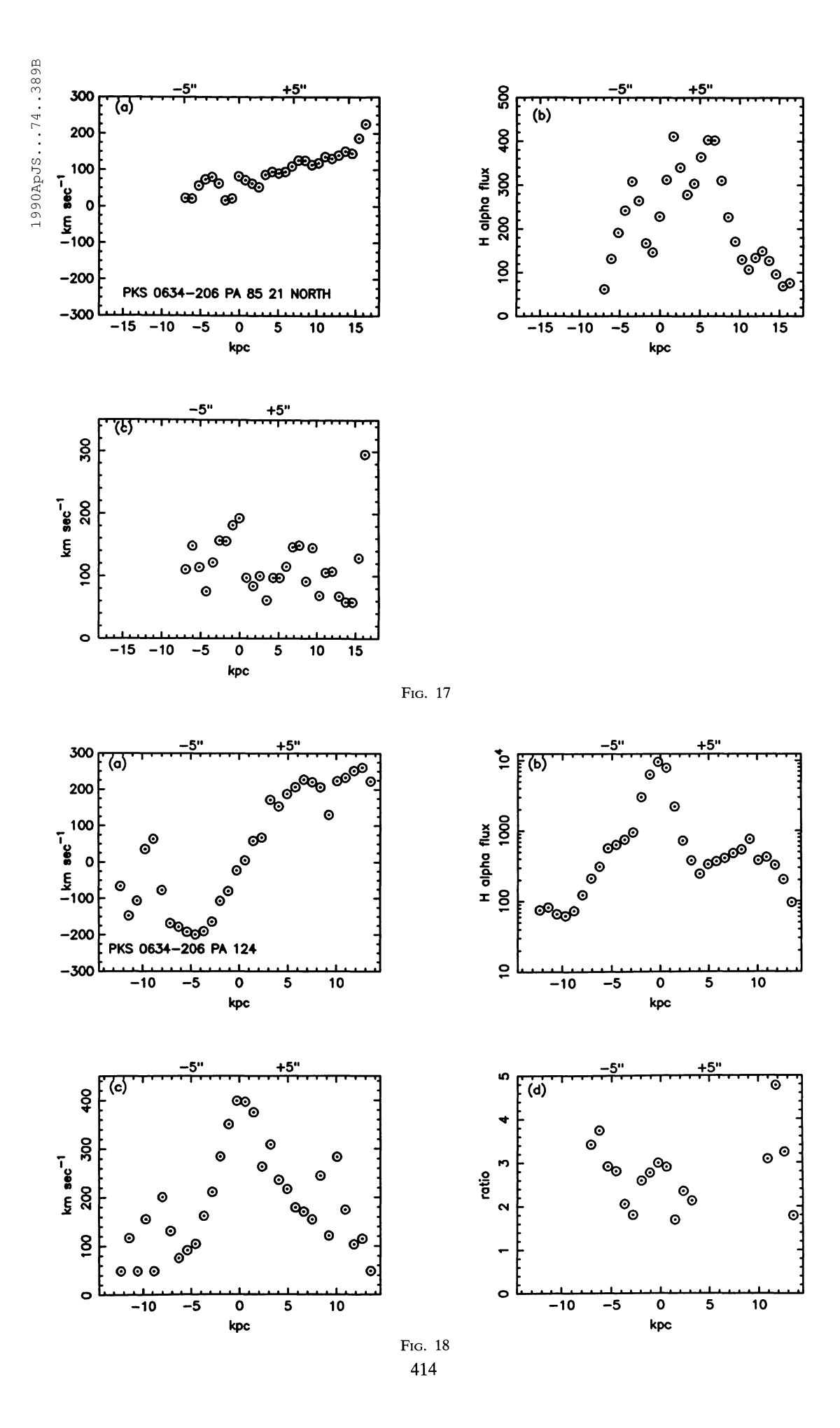
 \odot American Astronomical Society • Provided by the NASA Astrophysics Data System



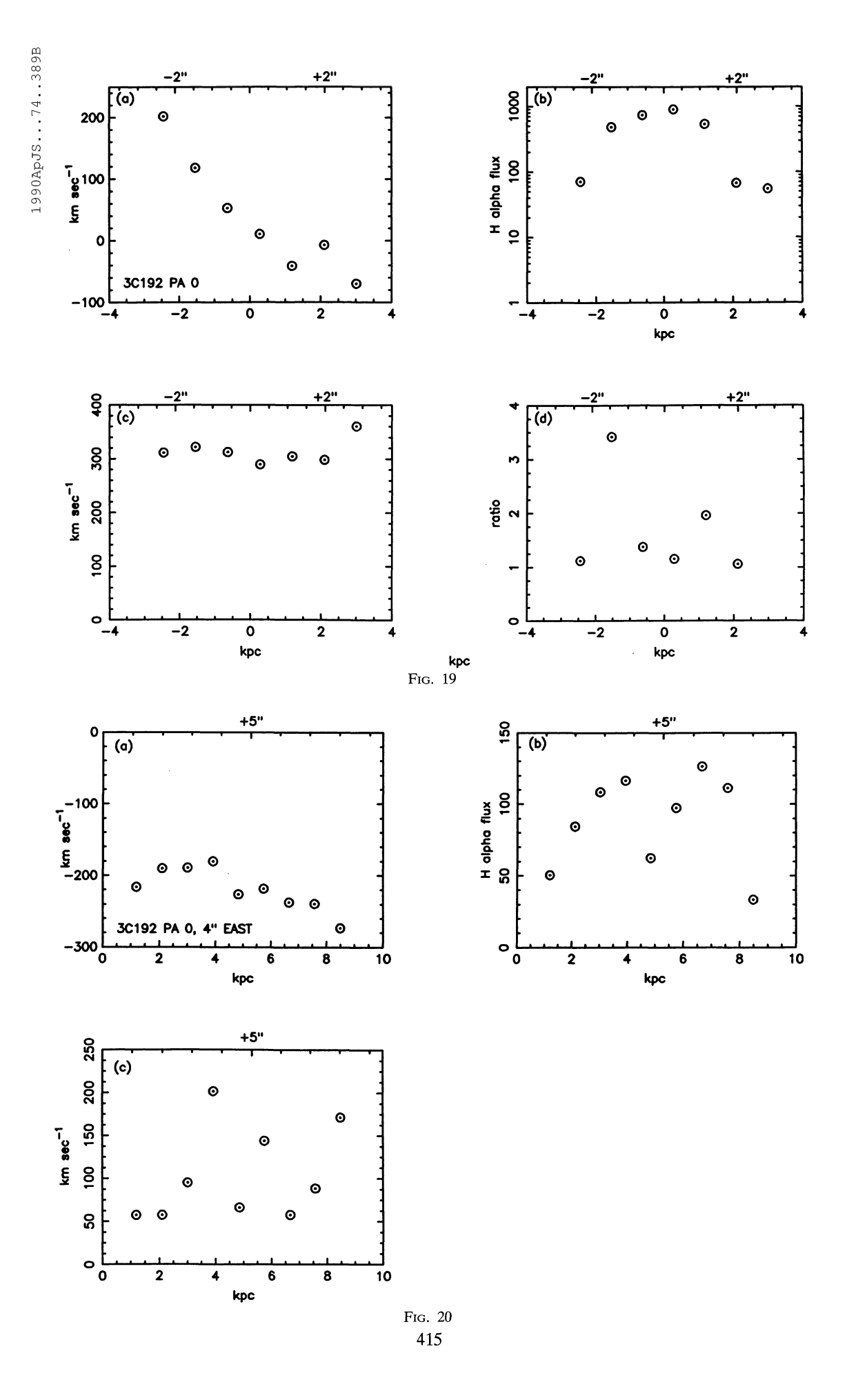
© American Astronomical Society • Provided by the NASA Astrophysics Data System



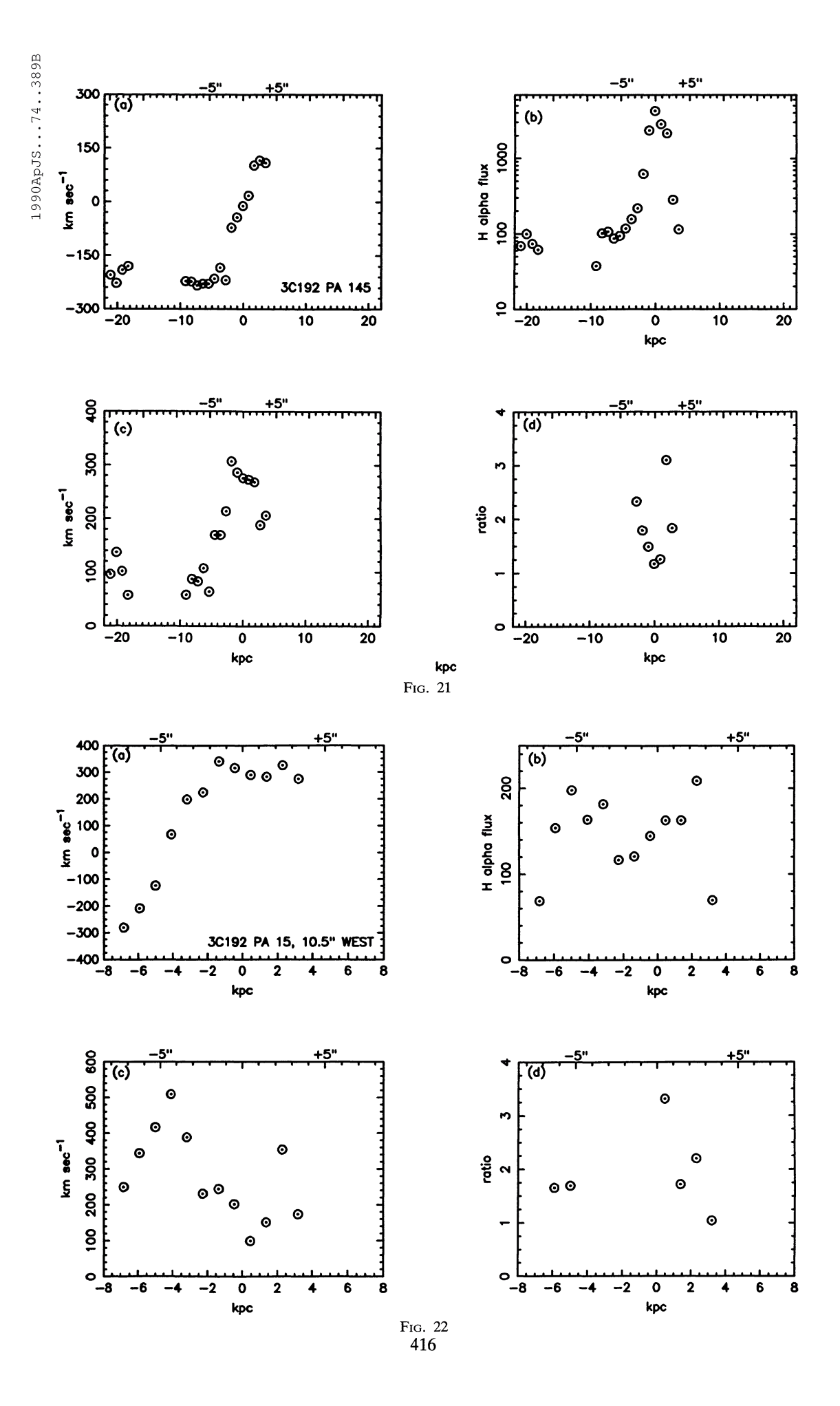
 \odot American Astronomical Society • Provided by the NASA Astrophysics Data System



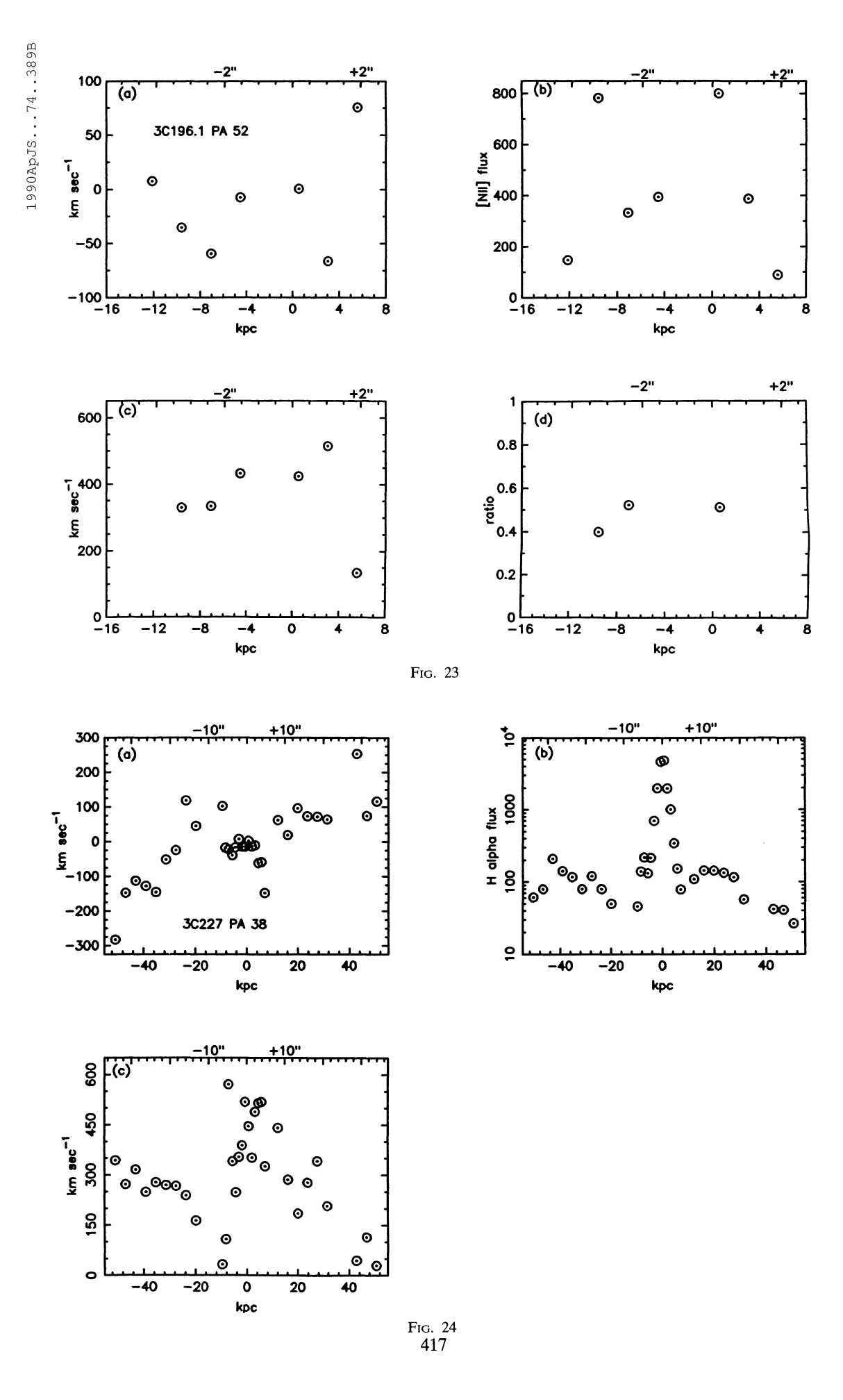
 \odot American Astronomical Society • Provided by the NASA Astrophysics Data System

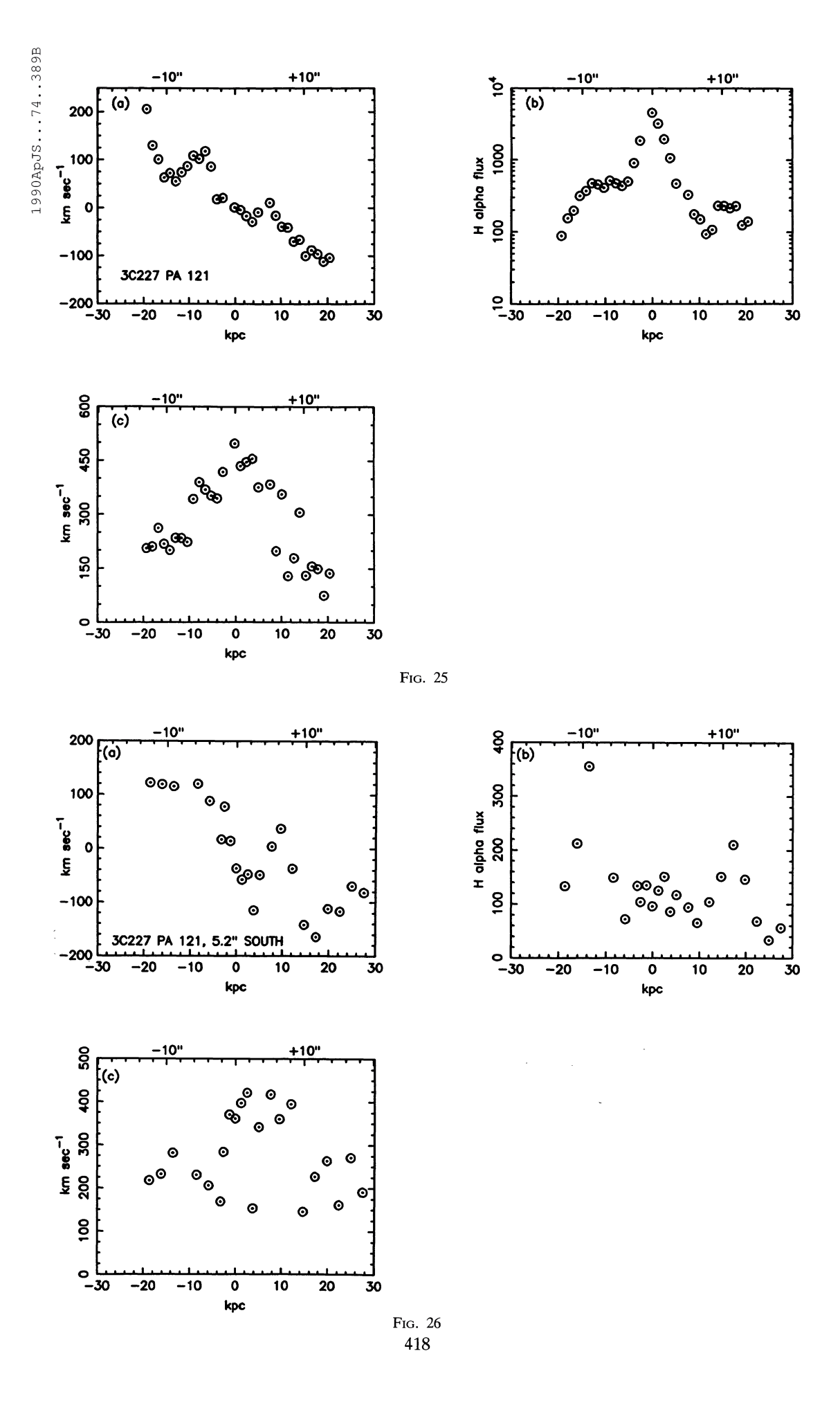


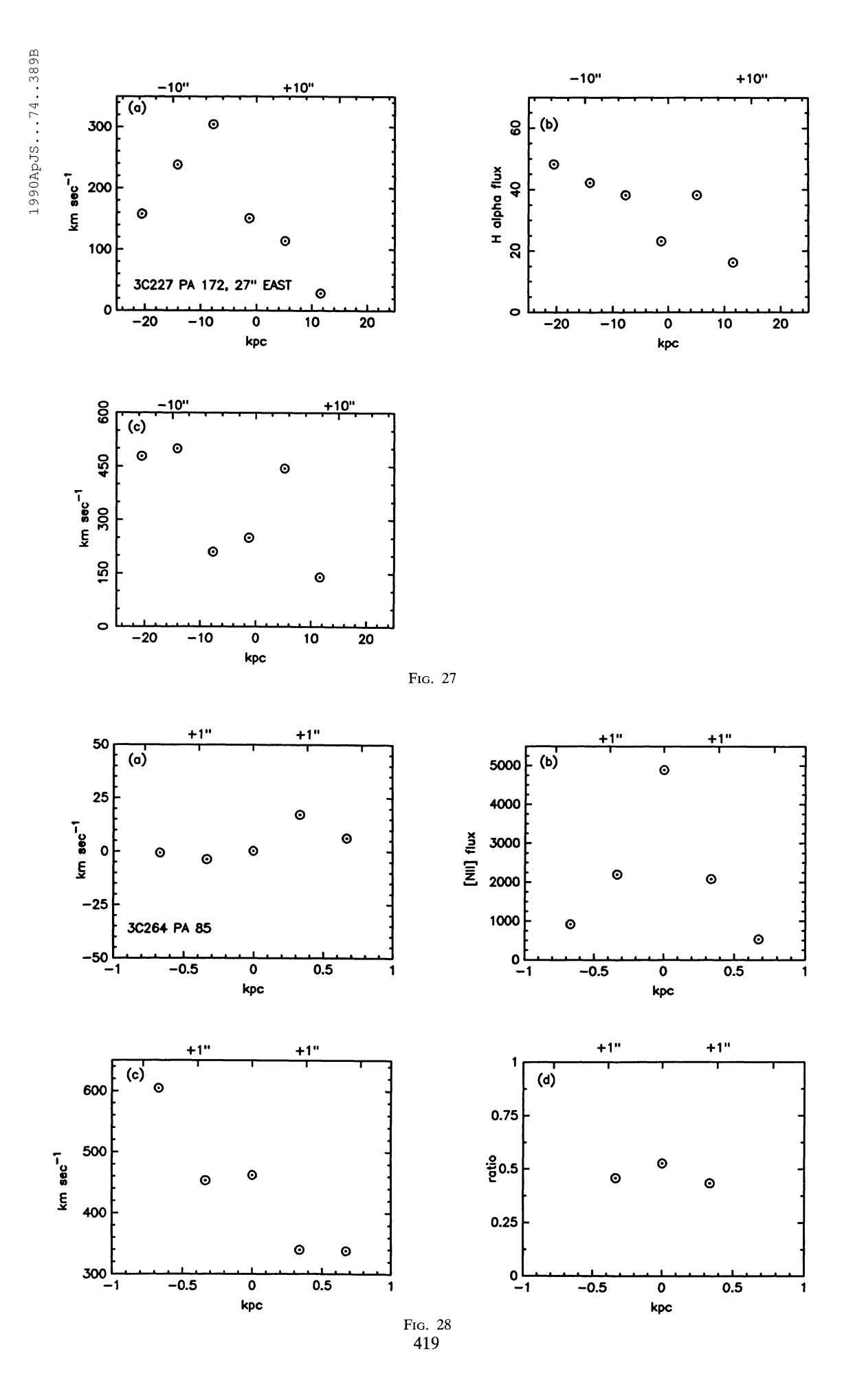
 ${\small \circledcirc \textbf{ American Astronomical Society \bullet Provided by the NASA Astrophysics Data System}}$



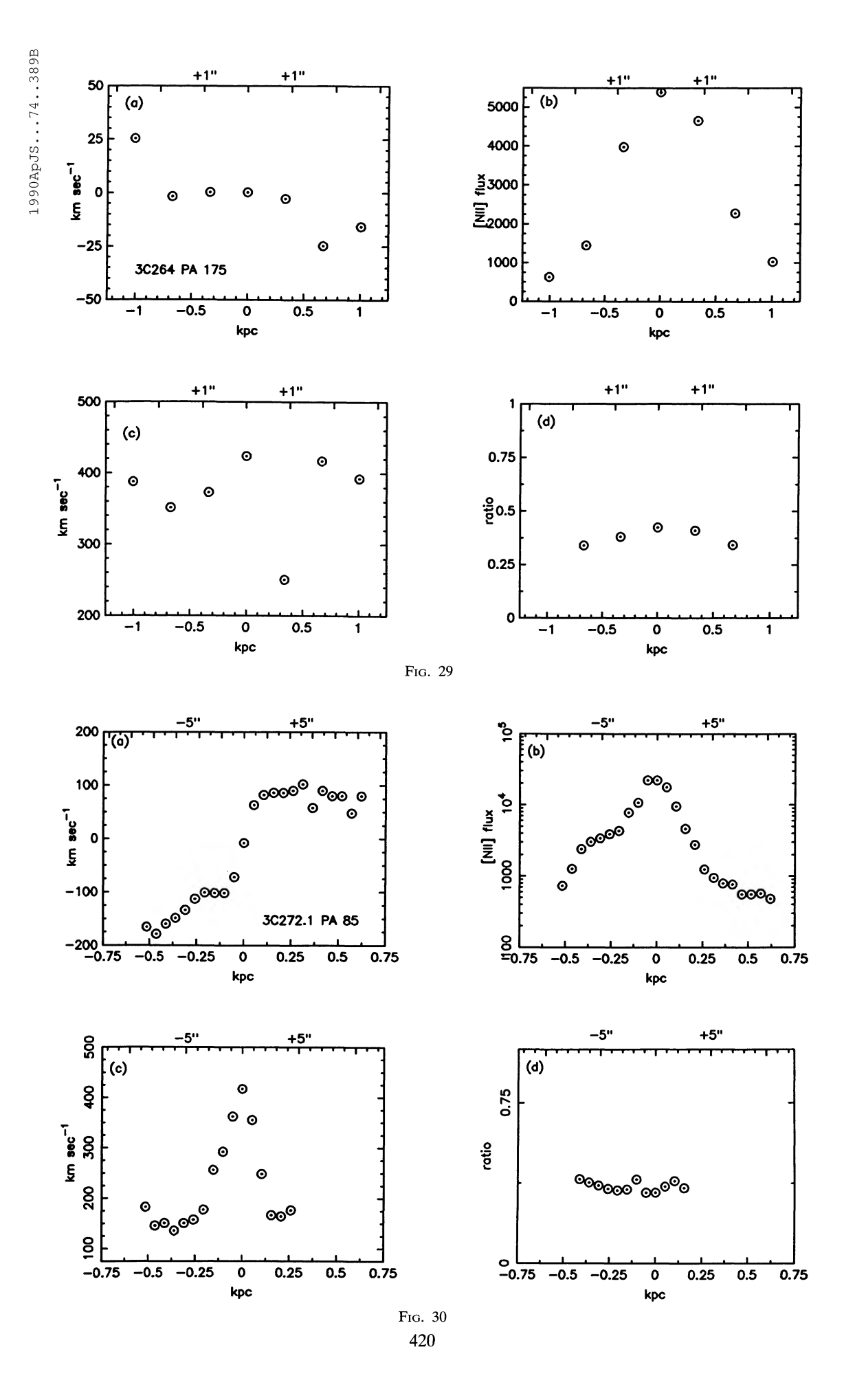
 \odot American Astronomical Society • Provided by the NASA Astrophysics Data System



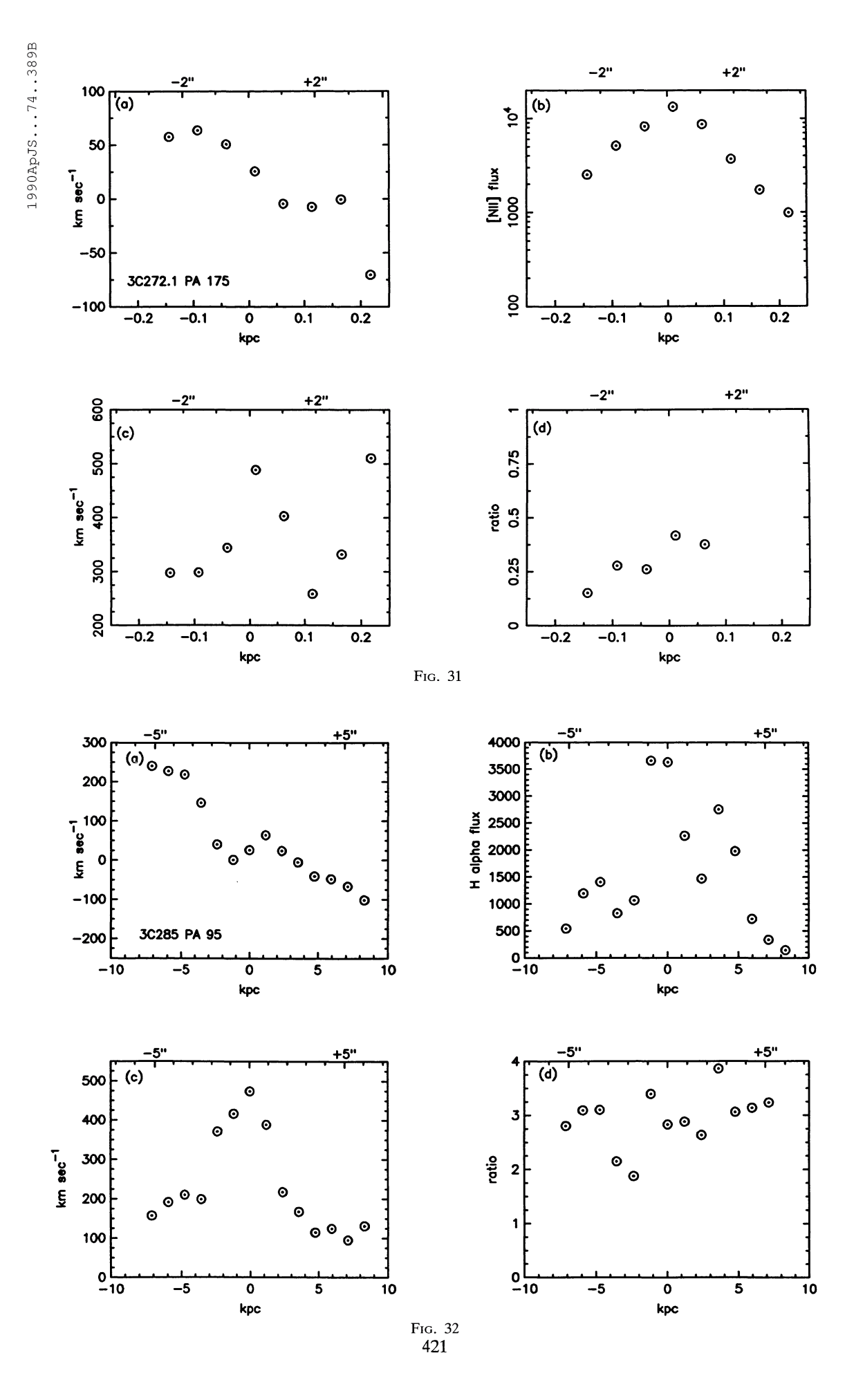




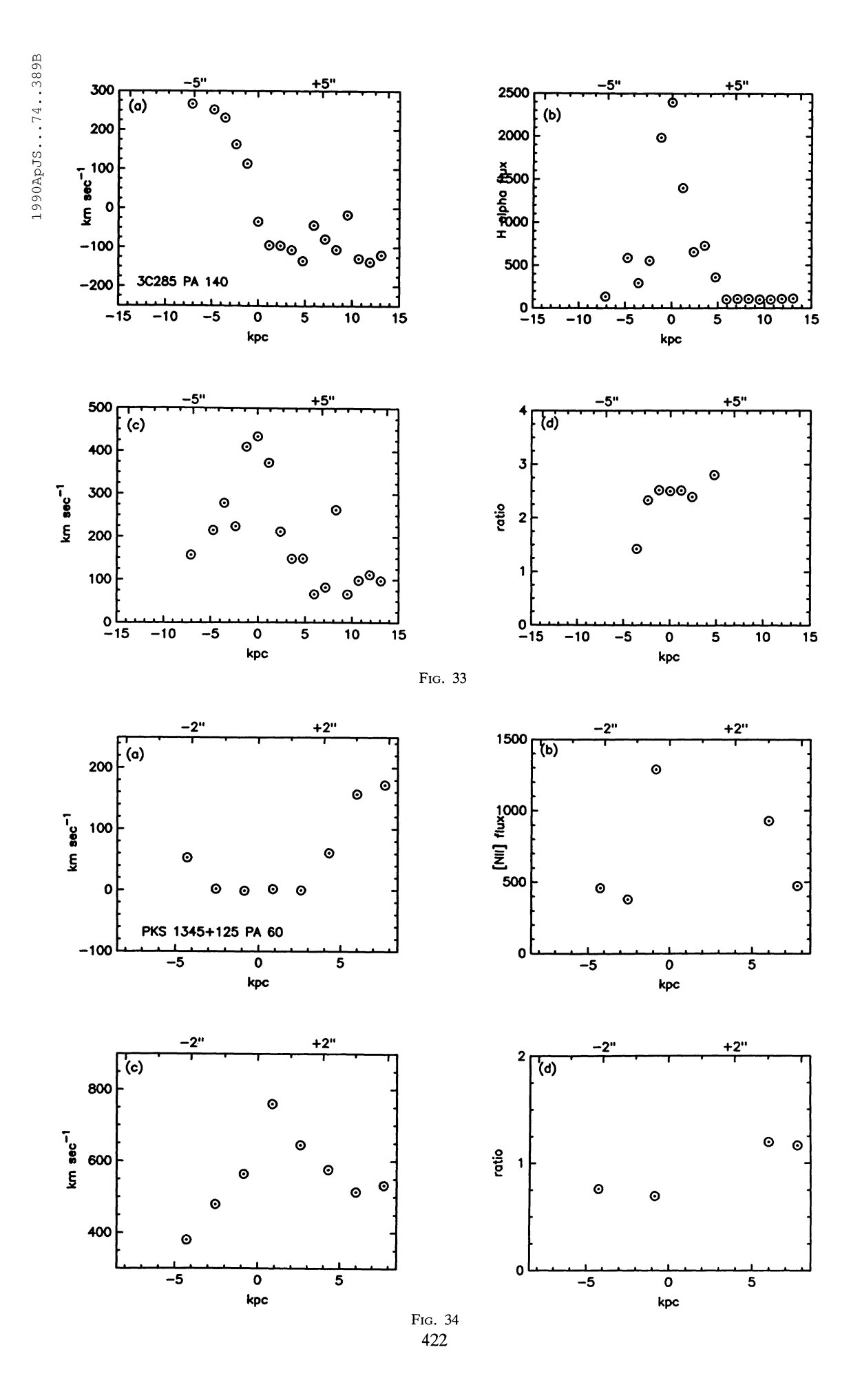
 \odot American Astronomical Society • Provided by the NASA Astrophysics Data System

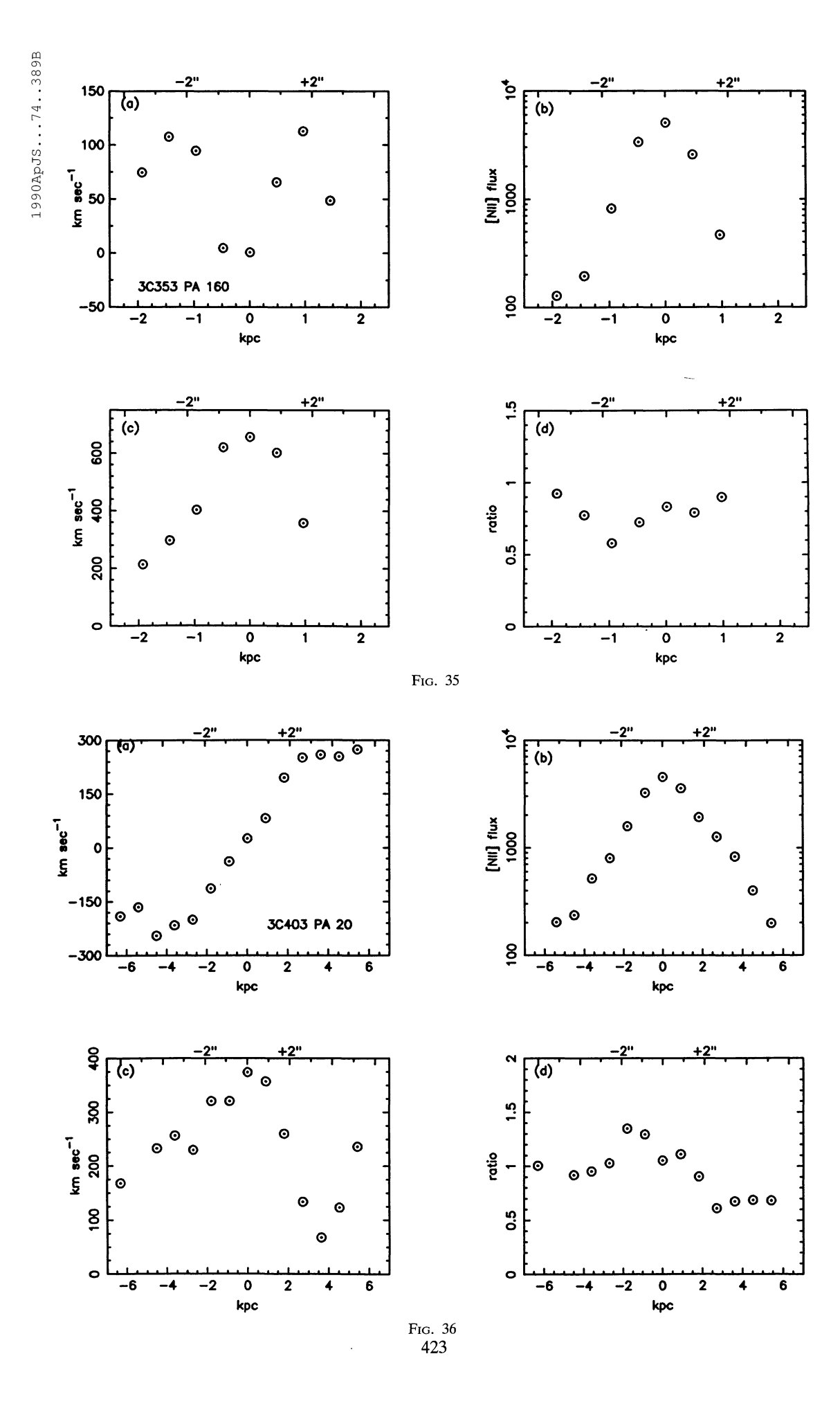


 \odot American Astronomical Society • Provided by the NASA Astrophysics Data System

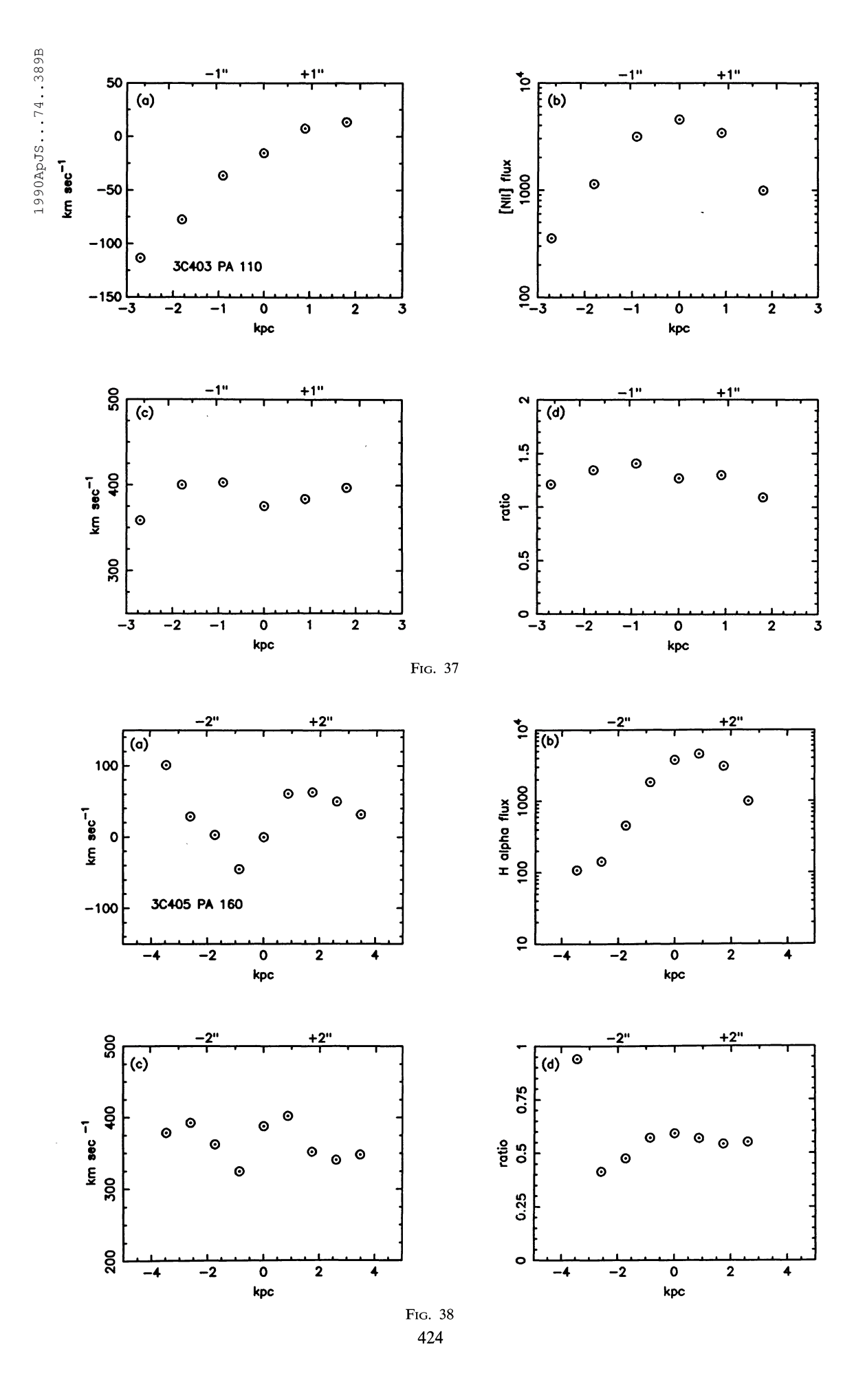


© American Astronomical Society • Provided by the NASA Astrophysics Data System

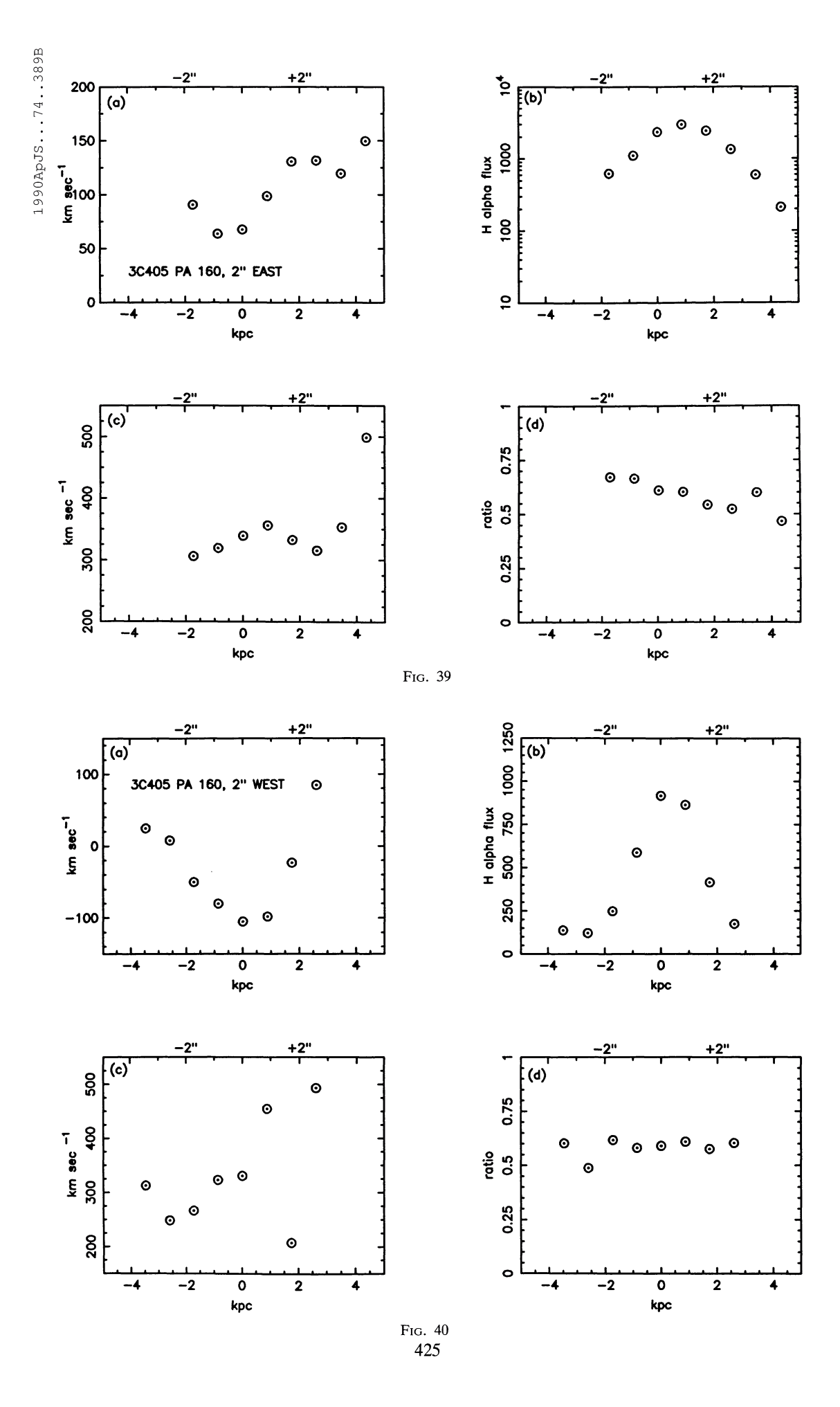




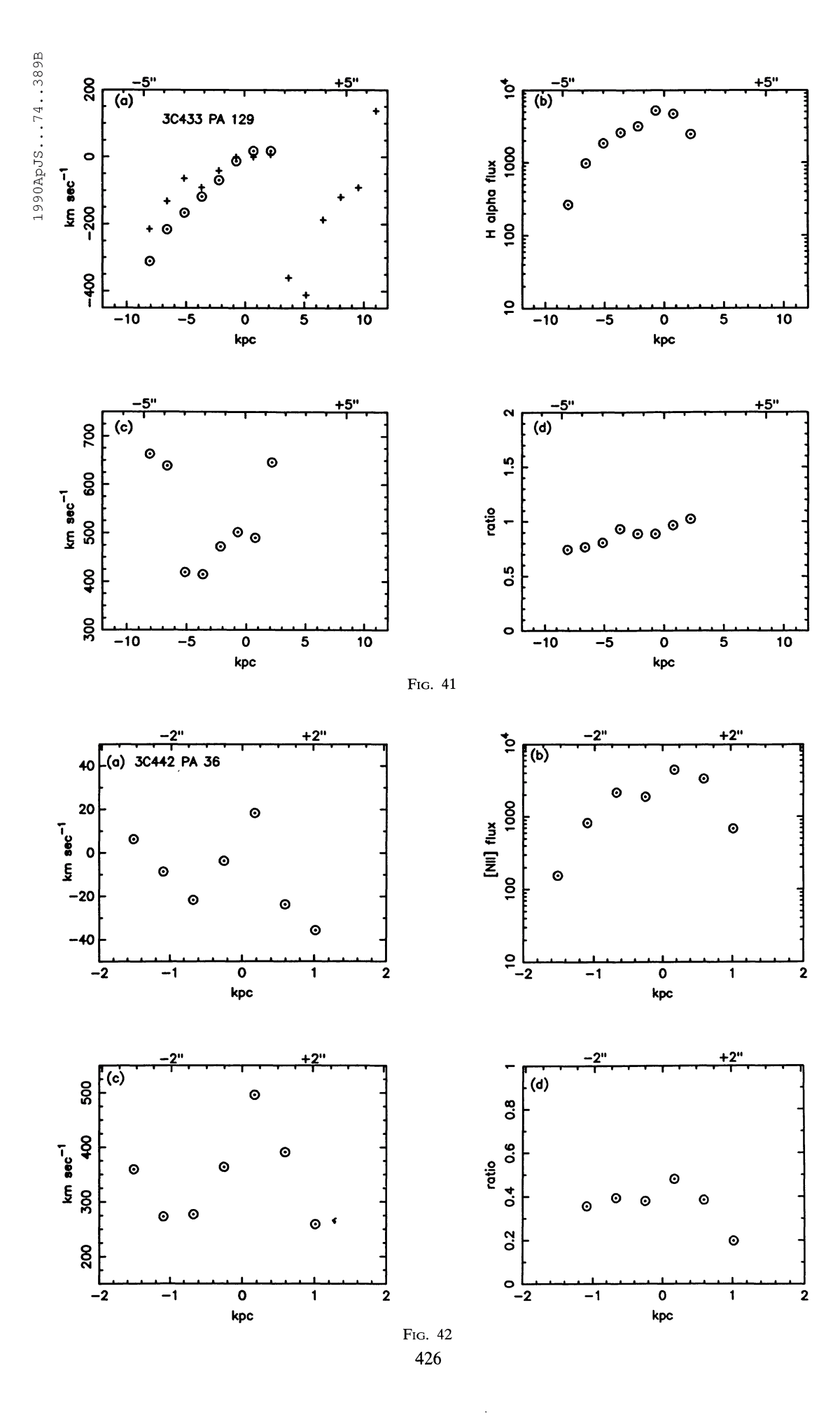
 $@ \ American \ Astronomical \ Society \ \bullet \ Provided \ by \ the \ NASA \ Astrophysics \ Data \ System$



 \odot American Astronomical Society • Provided by the NASA Astrophysics Data System



 \odot American Astronomical Society • Provided by the NASA Astrophysics Data System



 \odot American Astronomical Society • Provided by the NASA Astrophysics Data System

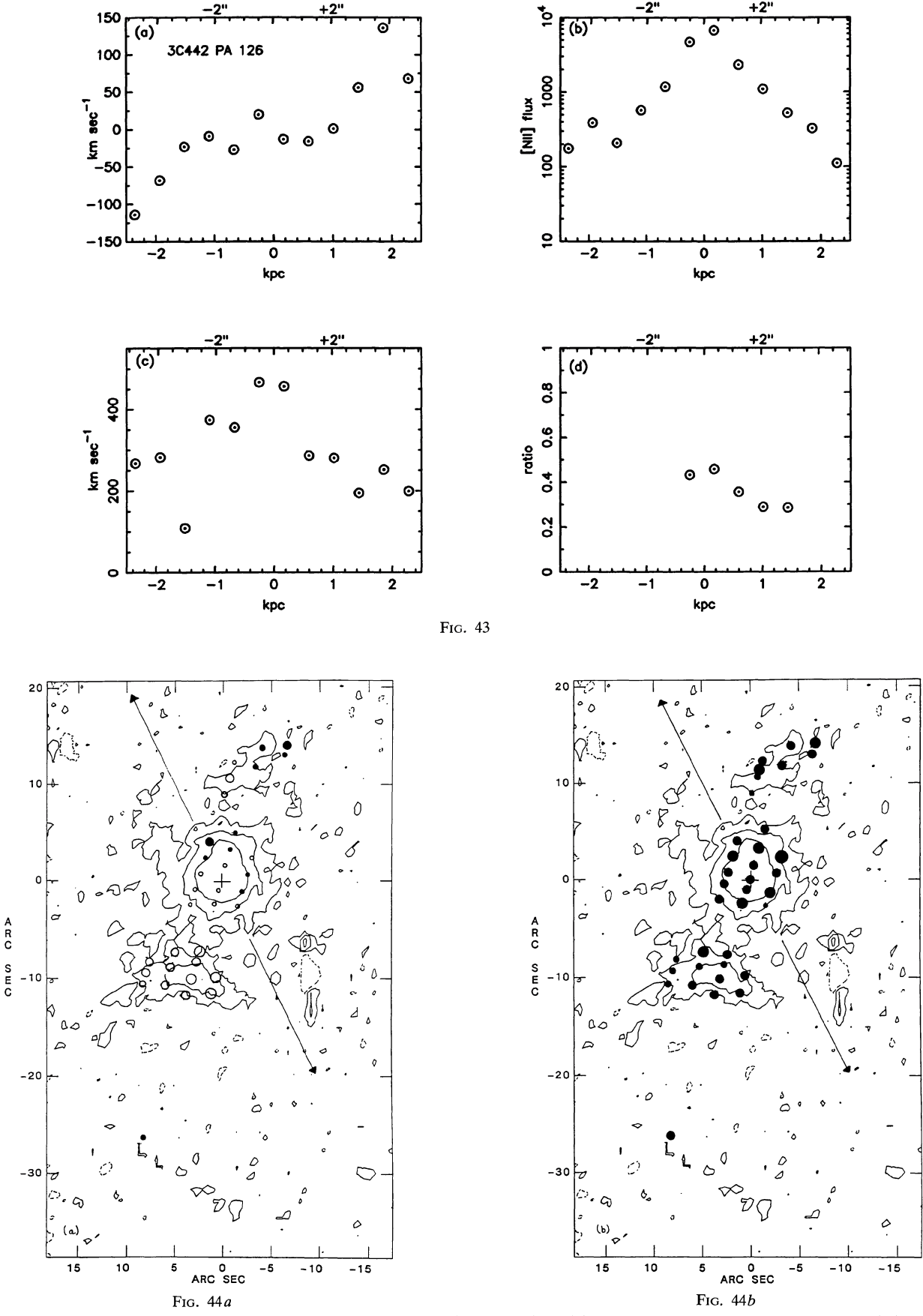


Fig. 44.—For 3C 98, superposed on contours of the emission-line flux (see Paper I) are (a) symbols whose size and tint indicate the relative velocity of the gas and (b) symbols whose size indicate the FWHM observed in the gas. See Table 43 for the symbol definition and § IV for a further description of the organization of this plot.

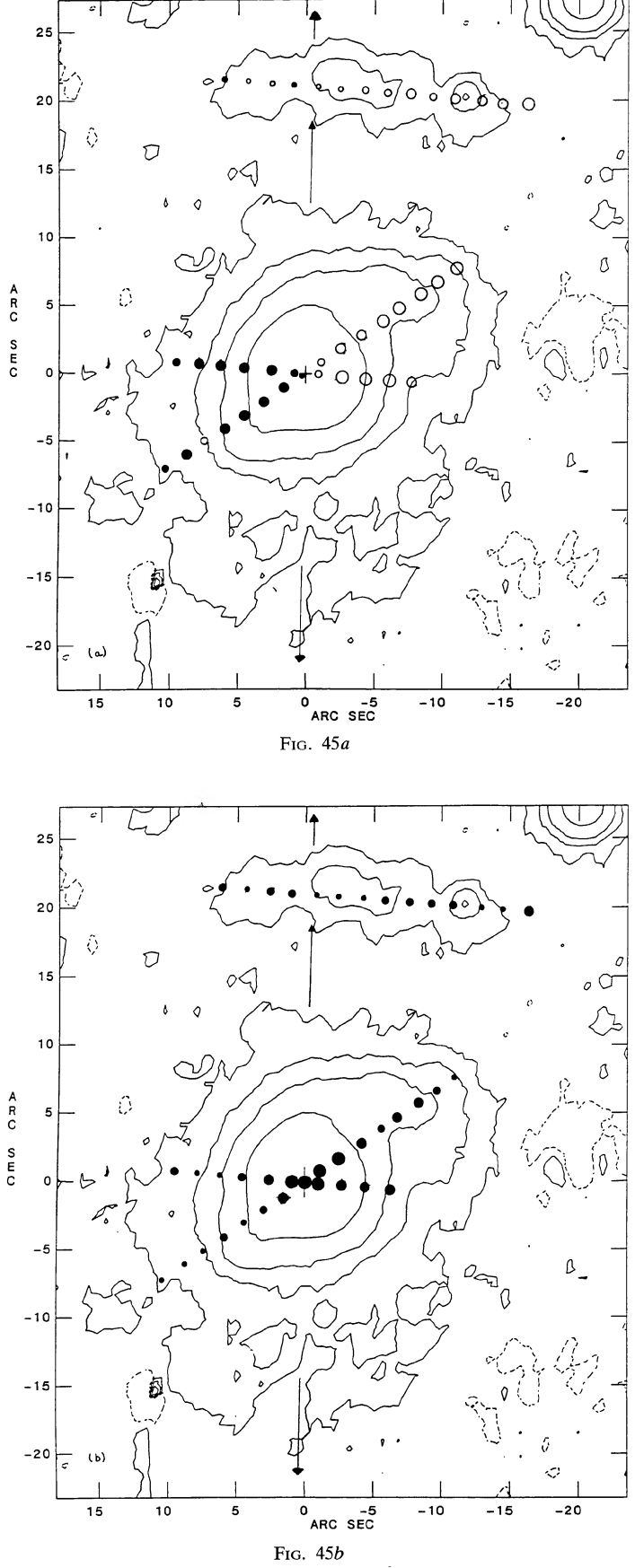


Fig. 45.—For PKS 0634-206, superposed on contours of the emission-line flux (see Paper I) are (a) symbols whose size and tint indicate the relative velocity of the gas and (b) symbols whose size indicate the FWHM observed in the gas. See Table 43 for the symbol definition and § IV for a further description of the organization of this plot.

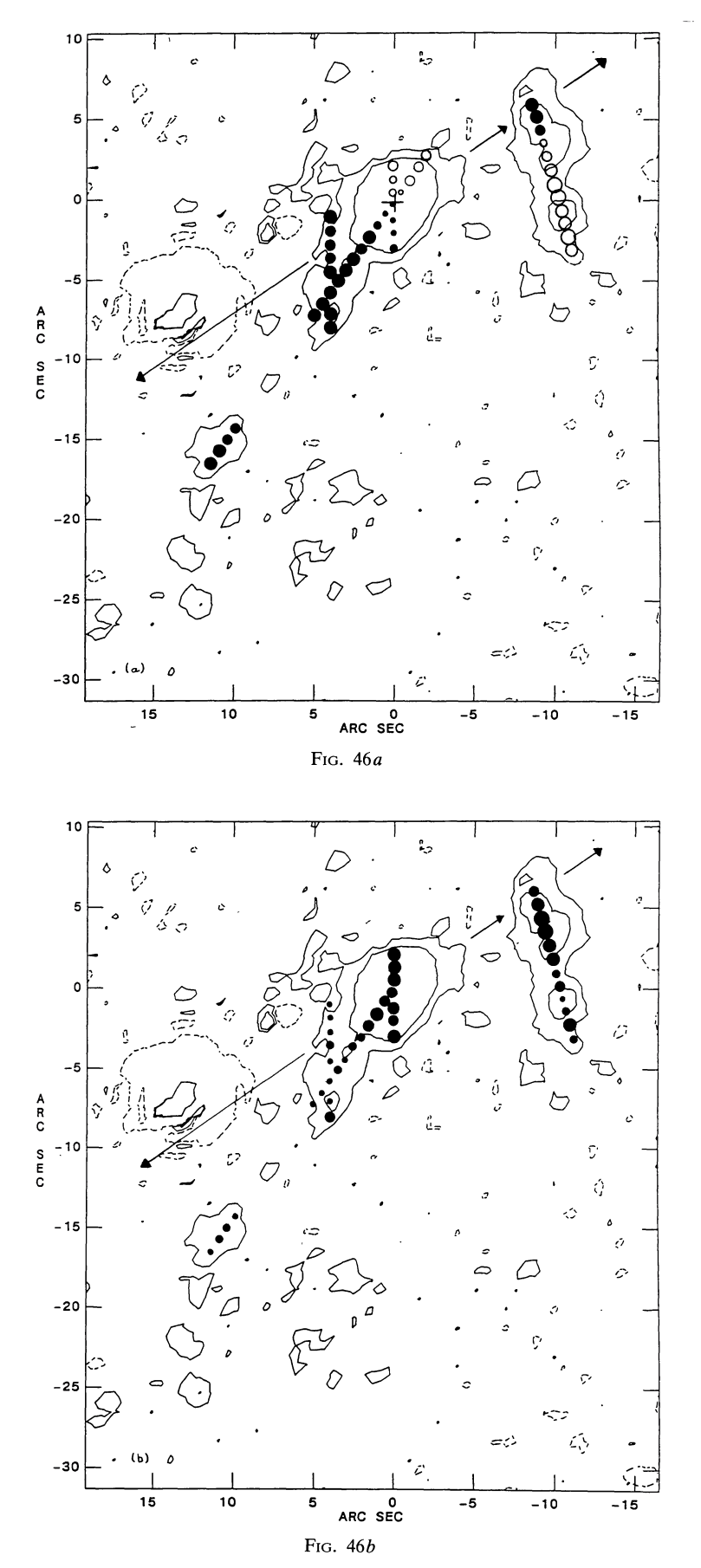


Fig. 46.—For 3C 192, superposed on contours of the emission-line flux (see Paper I) are (a) symbols whose size and tint indicate the relative velocity of the gas and (b) symbols whose size indicate the FWHM observed in the gas. See Table 43 for the symbol definition and § IV for a further description of the organization of this plot.

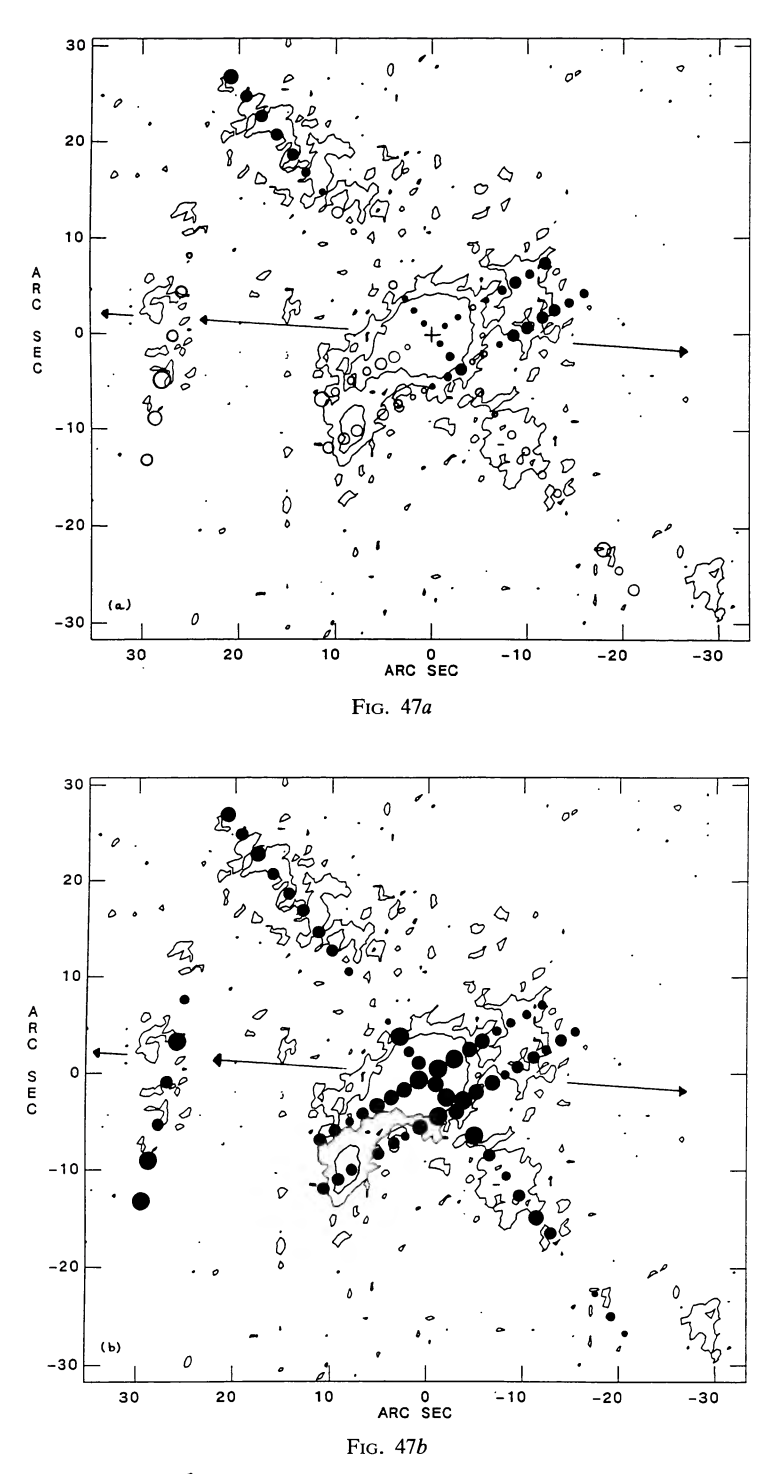


Fig. 47.—For 3C 227, superposed on contours of the emission-line flux (see Paper I) are (a) symbols whose size and tint indicate the relative velocity of the gas and (b) symbols whose size indicate the FWHM observed in the gas. See Table 43 for the symbol definition and § IV for a further description of the organization of this plot.

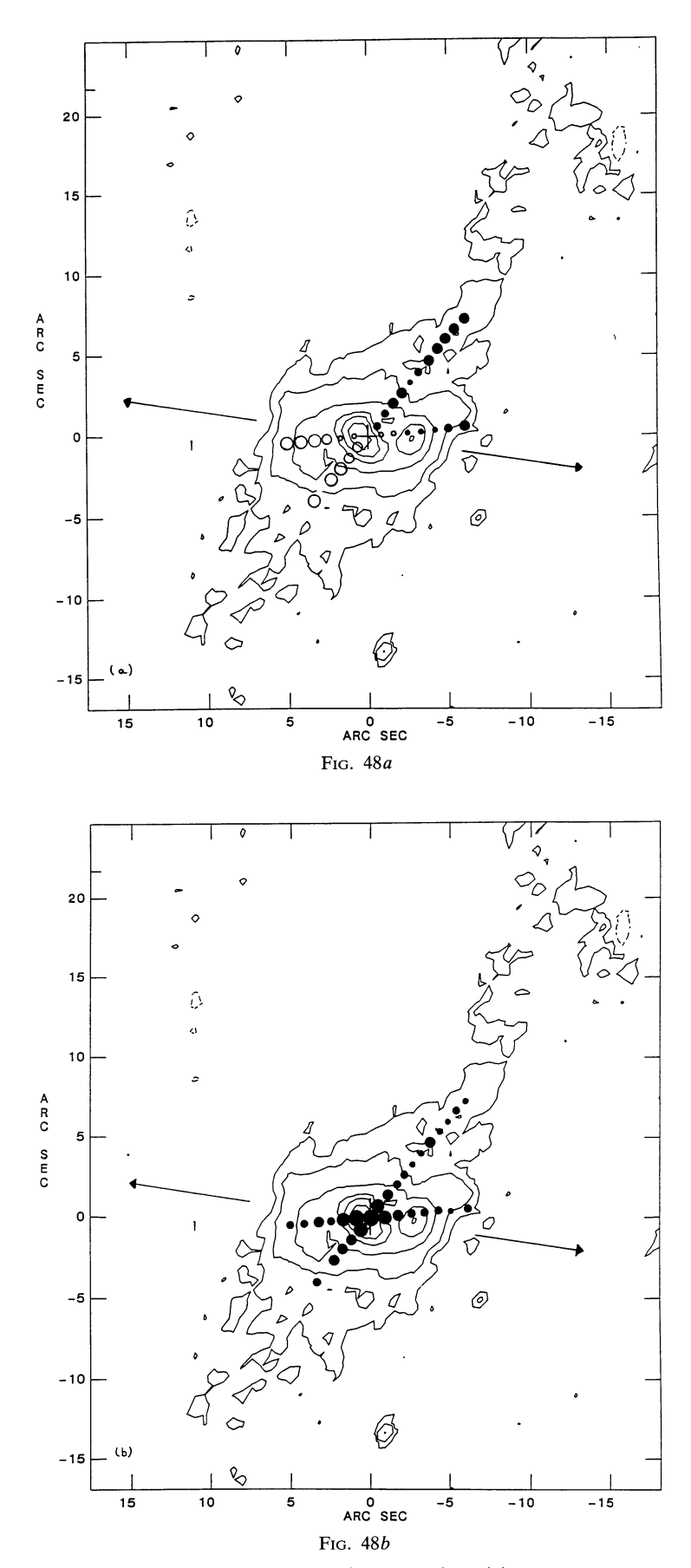


Fig. 48.—For 3C 285, superposed on contours of the emission-line flux (see Paper I) are (a) symbols whose size and tint indicate the relative velocity of the gas and (b) symbols whose size indicate the FWHM observed in the gas. See Table 43 for the symbol definition and § IV for a further description of the organization of this plot.

431

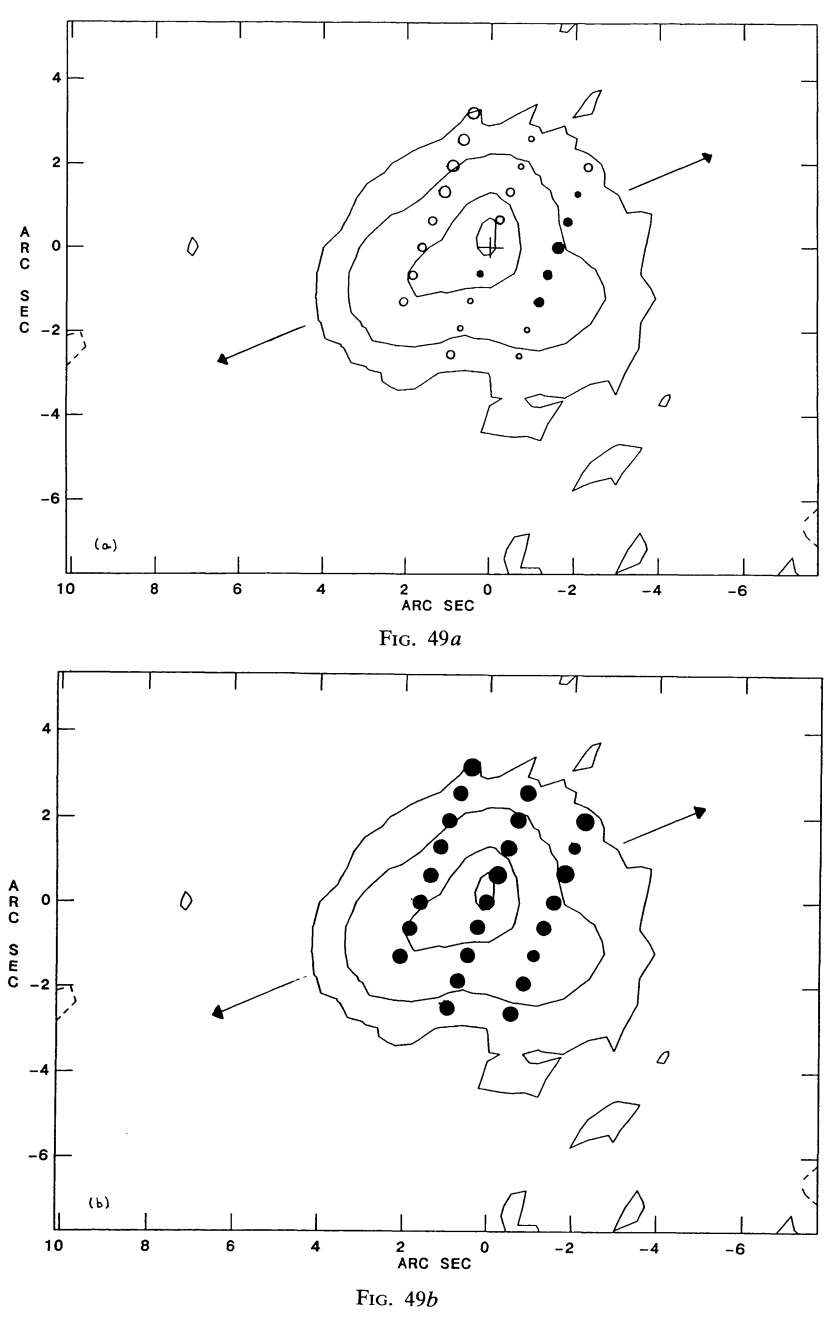


Fig. 49.—For 3C 405, superposed on contours of the emission-line flux (see Paper I) are (a) symbols whose size and tint indicate the relative velocity of the gas and (b) symbols whose size indicate the FWHM observed in the gas. See Table 43 for the symbol definition and § IV for a further description of the organization of this plot.

velocity different between the nucleus and the center of the disk rotation of $\sim 60 \text{ km s}^{-1}$. The nucleus thus appears to be blueshifted with respect to the mean of the off-nuclear gas. Thus, noncircular motions (e.g., outflow or inflow) are also likely to be present in the emission-line gas.

c) 3C 63

This galaxy shows an S-shaped region of emission-line gas whose western tail extends toward a continuum object. From our long-slit spectra we can discern no pattern of orderly motion in the gas but find a range of relative velocities

covering ~ 550 km s⁻¹, with broad line widths ($\sim 500-600$ km s⁻¹ FWHM) throughout the full extent of the emission-line nebula (i.e., at distances up to 20 kpc from the galaxy nucleus).

d) 3C 78

The host galaxy of 3C 78 has a small ($\sim 9''$, 5 kpc, in diameter), roughly circular, region of emission-line gas centered on its nucleus. Our spectra, obtained along three position angles separated by 60°, show no evidence of rotation with velocities greater than 50 km s⁻¹. We measure

TABLE 43 Key to Figures 44–49

Relative Velocity	Symbol	Velocity Width	Symbol
0 to -50 -51 to -100 -101 to -200 -201 to -300	:	0 to 100 101 to 200 201 to 300 301 to 400	•
< -300 1 to 50	•	> 400	
51 to 100	0		
101 to 200	0		
201 to 300	0		
> 300	0		

Notes.—Symbols apply to Figs. 44–49. In these figures, the superposed circles in (a) are the relative velocities (see cols. [1] and [2]) and in (b) are the FWHM line widths (see cols. [3] and [4]). All velocities are given in km s⁻¹, in the rest frame of the galaxy. Symbols in the figures are a factor of 2 smaller than those in this table.

broad line widths throughout the nebula of ~ 500 km s⁻¹ FWHM.

e) 3C 88

This source has a small [5" (3 kpc)] flattened emission-line nebula. We obtained spectra at three position angles separated by 60°. We find no evidence for organized motions but find that all of the gas within 2 kpc of the nucleus has a velocity within 50 km s $^{-1}$ of the velocity of the nuclear gas. Line widths are 400–500 km s $^{-1}$ (FWHM) on the nucleus and drop to 200–300 km s $^{-1}$ (FWHM) within 1 kpc of the nucleus.

We have attempted to map the kinematic properties in the very extended region of emission-line gas in this radio galaxy by stepping the slit (held in position angle 163°) across the nebula in steps of 2".5. Figures 44a and 44b show, respectively, the outline of the emission-line region presented in Paper I, with numbers superposed indictating, respectively, the measured relative velocities of the gas and FWHM of the emission lines. We find no evidence for rotation of the gas in the inner 3" (3 kpc) (all velocities within ~ 50 km s⁻¹ of the nuclear velocity) and relatively narrow line widths for both the nuclear gas and the more extended gas ($\sim 300 \text{ km s}^{-1}$ FWHM). The velocity pattern of the more extended emission-line gas is more difficult to trace, showing deviations of up to $\pm \sim 200$ km s⁻¹ from the nuclear velocity, with an overall tendency to be positive on one side of the nucleus and negative on the other. If this extended gas is in ordered rotation, then there must be large deviations from simple circular motions.

Note also the *rise* in the H α to [N II] ratio observed in the emission-line gas which is ~ 7 kpc out from the nucleus.

g) PKS 0634-206

The emission-line nebula in this galaxy is very extended (40", 40 kpc) and quite complex (see Paper I, and references

therein). We obtained two spectra with the split passing through the nucleus, along position angles 85° and 124°; Tadhunter, Fosbury, and Quinn (1989) obtained spectra passing through the nucleus along position angles 170°, 145°, and 135°. The gas near the nucleus appears to be in rotation with a measured maximum rotational velocity of ~275 km s⁻¹ along PA 135. A "best fit" to the observed maximum velocities along position angles 85, 124, 135, and 178 gives a rotational axis of 31°, and an inclination angle of 34°, assuming the gas is on circular orbits in a flattened disk. However, the residuals on the fit are high, suggesting that noncircular motions, perhaps infall or outfall, are also present. Along most position angles the rotation curve flattens at a radial distance of ~3 kpc, although along position angle 135° the rotation curve does not appear to turn over until ~ 8 kpc. The gas ~ 8 kpc out along PA 124 shows evidence for large deviations from circular motions ($\Delta v \sim 250 \text{ km s}^{-1}$), on both sides of the nucleus.

In addition, we obtained a third spectra of the nebula with the slit spectra offset from the nucleus and passing through the arc of emission-line gas located (21", 21 kpc) north of the nucleus (see Fig. 45). This arc of gas is oriented tangentially to the radial from the nucleus. The position angle of the large-scale radio source passes directly through, in projection, the center of this arc. On Figure 45, we have indicated with an arrow the projected location of the radio axis with respect to the emission-line gas. We find no evidence (in the form of a steep velocity gradient or broad line widths) that the emission-line gas and the radio source are interacting. Rather we find a rather smooth progression of velocities along the filament of 140 km s⁻¹ over 22 kpc (i.e., \sim 6 km s⁻¹ kpc⁻¹). The measured line widths in the "arc" are small, \leq 60–175 km s⁻¹ FWHM.

h) 3C 192

The emission-line nebula in 3C 192 is complex and quite extended (18 kpc). We obtained slit spectra at three position angles passing through the nucleus and two additional positions offset from the nucleus, designed to pass through the more filamentary emission (see Fig. 46). Along PA 145 the gas appears to show a characteristic rotation curve, with a rotational velocity of 175 km s⁻¹ and a flattening of the curve at a distance ~ 4" (2 kpc) from the nucleus. Unfortunately, line emission was detected to only a distance of 2 kpc to the west of the nucleus. However, based on the available data, the rotation centroid of the rotation curve appears to be offset by 1".5 (1.5 kpc) from the nucleus, corresponding to a velocity difference of $\sim 60 \text{ km s}^{-1}$ with respect to the nuclear gas. The nucleus thus appears to be redshifted with respect to the average velocity of the off-nuclear gas. The widths of the lines drop rapidly with distance from the nucleus in most places, from $\sim 300 \text{ km s}^{-1} \text{ FWHM}$ on the nucleus to less than 70-100 km s⁻¹ at a distance of 6 kpc. Note also the rapid rise of the H α to [N II] ratio with increasing distance from the nucleus along PA 145.

The slit located 10.75 west of the nucleus along position angle 15° was positioned in order to map the velocity field along a tangential filament, running perpendicular to the direction of the radio source axis and intercepted by that axis. The location of the projection of the radio source axis

on the filament is indicated with an arrow in Figure 46. We find that at this location there is a rapid gradient in the velocities of the emission-line gas. The velocities fall from $\sim +300$ to ~ -300 km s $^{-1}$ within a distance of ~ 5.5 kpc (corresponding to a gradient of ~ 110 km s $^{-1}$ kpc $^{-1}$). The line widths increase sharply at the location of the intersection (from 200 to 500 km s $^{-1}$), returning to 200 km s $^{-1}$ at the measured end of the filament.

i) 3C 196.1

The slit was aligned along the radio source axis which is coincident with the major axis of the emission-line nebula. We can discern no ordered kinematics in the gas in this nebula, but find all velocities within 75 km s⁻¹ of the nuclear velocities and line widths of $\sim 400 \text{ km s}^{-1}$ (FWHM).

j) 3C 227

The emission-line nebulae in 3C 227 is the largest seen in any of the radio galaxies in our sample. It extends over 100 kpc end to end. We obtained four slit positions on this galaxy in an attempt to map the kinematics of the near nuclear emission-line gas as well as the kinematics of the off-nuclear filaments. In Figure 47 we show a contour map of the $H\alpha + [N\ II]$ emission with the velocities and velocity widths of the gas superposed.

The two slit positions which pass through the nucleus both show gradients of $\sim 200 \text{ km s}^{-1}$ over 20 kpc (i.e., a gradient of only $\sim 10 \text{ km s}^{-1}$ kpc), with positive velocities on one side of the nucleus and negative velocities on the other. However, large deviations from this gradient are seen. Along PA 121, at ± 10 kpc deviations of order 75 km s⁻¹ (both in the same sense) are seen, while along PA 38, at ± 10 kpc, deviations of order 100 km s⁻¹ are seen. In addition, no flattening of the "rotation curve" is observed, even at distances of 20–40 kpc from the nucleus. Thus, it is not clear that the observed gradual gradient of velocities is indeed rotational.

As can be seen in the spectra taken along PA 38, and in the spectra taken with the slit positioned off-nucleus, even in the most extended emission-line gas (20–40 kpc from the nucleus), the emission lines appear to be resolved, with widths of $\sim 200-300$ km s⁻¹. Interaction of the backflowing radio plasma and the emission-line gas may be responsible for maintaining turbulence in the gas so far from the galaxy nucleus. Unfortunately, the signal to noise in these very distant lines is very low. However, this is a potentially important result which should be confirmed.

k) 3C 264

The emission-line nebula in 3C 264 is small (6".3, 2.4 kpc), centrally condensed, and approximately oval in shape. We have obtained slit spectra along two position angles (PA 175 and PA 85) separated by 90°. We find no gas with velocities relative to the nucleus of more than 50 km s⁻¹ along either position angle, and no evidence for any systematic gradients across the nucleus. We measure line widths across the nebula of $\sim 400 \text{ km s}^{-1}$.

l) 3C 272.1 (M84)

Our long-slit spectra were taken along the major and the minor axes of the small (24".5, 1.5 kpc), flattened, S-shaped emission-line nebulae in the heart of M84. We find a "characteristic" rotation curve in the inner parts of the nebula. Along the major axis of the nebula (PA 85), the velocities reach a maximum of ~ 100 km s⁻¹ at a radial distance of ~ 0.1 kpc (~ 1 ".7), and then flatten. This corresponds to a gradient of $\sim 1000 \text{ km s}^{-1} \text{ kpc}^{-1}$! If this represents rotation about the nucleus, then the mass in the inner 100 pc is $\sim (2 \times 10^8)(\sin^2 i)^{-1} M_{\odot}$. Along this position angle, the gas beyond 0.25 kpc to the east of the nucleus shows a second systematic velocity gradient, reaching a velocity difference of ~ -200 km s⁻¹ at r = 0.5 kpc, while to the west, the velocity curve remains flat. Along PA 175 (the minor axis of the nebula and the radio source axis), we also observe a characteristic rotation curve, with a amplitude of 40 km s⁻¹ reached in the inner 0.1 kpc (a gradient of $400 \text{ km s}^{-1} \text{ kpc}^{-1}$). However, the rotation curve is highly displaced with respect to the nucleus, reaching $\sim +60 \text{ km s}^{-1}$ to the south, and only -5 km s^{-1} to the north of the nucleus. Thus the nucleus appears to be slightly blueshifted with respect to the off-nucleus gas. Combining the measured values of $v_{\rm rot}$ at the two position angles gives a rotation axis of 0° (or roughly aligned with the radio axis) and a inclination angle of 54°, assuming circular rotation of gas in a disk. The line widths are broad on the nucleus ($\sim 400 \text{ km s}^{-1}$) but narrow rapidly with increasing distance, reaching $\sim 150 \text{ km s}^{-1}$ at a distance of 0.2 kpc.

m) 3C 285

The emission-line image of 3C 285 shows two systems of gas; one a bright S-shaped region of gas oriented along the radio source axis (PA 95), and the second running virtually perpendicular to the first, of much lower surface brightness and appearing to connect with a companion galaxy 26" (35 kpc) to the north. Along both position angles, our long-slit spectra show that the gas velocities are positive on one side of the nucleus and negative on the other, consistent with circular rotation of the gas about the nucleus (see Fig. 48). However, along the jet axis (PA 95), the directional sense of the gas velocities in the inner few kiloparsecs is reversed with respect to the rotational sense of the gas further out. Along PA 140, the velocities of the gas northeast of the nucleus flatten within 1 kpc of the nucleus, while to the southeast the "rotation" curve does not flatten until beyond 4 or 5 kpc. Thus the "rotation curve" is quite asymmetric with respect to the nucleus.

n) PKS 1345+125

This galaxy has a double nucleus, with the northwestern nucleus showing line emission. Off-nuclear line emission with a total extent of $\sim 8''$ (15 kpc) can be seen in the form of an extension to the northeast and a tail of emission extending to the southeast and curving westward. We located the slit on this northwesterly nucleus, at PA 60. We find no evidence that the gas is in rotation. The gas within ~ 5 kpc of the nucleus has a velocity within ~ 60 km s⁻¹ of the velocity of

1990ApJS...74..389

the nuclear gas, and the most distant gas southwest of the nucleus shows high positive velocities. The forbidden line widths are very broad on the nucleus and remain broad throughout the emission-line region ($\sim 400{-}600~\rm km~s^{-1}$ FWHM).

o) 3C 353

This galaxy has a small, oval region of emission-line gas centered on its nucleus with a diameter of $\sim 7^{\prime\prime}.5$ (4 kpc). We placed our slit along the long axis of this nebula and find no systematic motions in the gas, with the velocities rising with respect to the nucleus both north and south of the gas, with an amplitude relative to the nucleus of 100 km s $^{-1}$. Thus, the velocity of the nuclear gas is blueshifted with respect to the mean of the extended gas. The line widths in the center are broad (600 km s $^{-1}$ FWHM) and drop rapidly (to ~ 200 km s $^{-1}$ FWHM) by 2 kpc.

p) 3C 403

The emission-line nebula in this galaxy comprises an oval region of gas, elongated along PA 33, from which protrudes a small, curved tail extending along the same position angle. Our long-slit spectra run along the major and minor axes of the nebula. The gas along the major axis shows a characteristic symmetric rotation curve with a rotational velocity of $\sim 220~\rm km~s^{-1}$, reached at $\sim 2~\rm kpc$ from the nucleus and a flattening of the curve thereafter. The nuclear line widths are $\sim 350~\rm km~s^{-1}$, dropping to $100-200~\rm km~s^{-1}$ within 2 or 3 kpc. Along the minor axis, the measured velocities of the gas are all within $\sim 100~\rm km~s^{-1}$ of the nuclear velocity, with a slight sloping of the velocities from east to west across the nucleus. The line widths along the minor axis remain at

350-400 km s⁻¹ (FWHM) throughout the ~ 5 kpc lateral extent of the nebula.

q) 3C 405

We have attempted to "map" the properties of the small, amorphous, emission-line region on the center of the Cygnus A radio galaxy by stepping the slit (held in PA 160) across the nebula in steps of 2". Figure 49 shows an outline of the emission-line nebula with the measured velocities and line widths superposed. We find a rather amorphous velocity pattern for the gas, with all measured velocities within ~ 150 km s⁻¹ of the velocity of the nuclear gas and no systematic motions apparent (see also Pierce and Stockton 1986). Measured line widths are predominantly in the range of $\sim 300-400$ km s⁻¹ (FWHM) throughout, with no strong drop in width off the nucleus. Simkin (1977) measured a strong velocity gradient in the emission-line gas along a slit passing through the nucleus along PA 25. We have insufficient data to confirm (or deny) this. Based on our current data we find no evidence for rotation.

r) 3C 433

Our emission-line image shows nuclear emission plus an elongated, slightly curving filament with an extent of ~ 22 kpc, pointing along a position angle which is askew by 36° to the radio source axis. We oriented our slit along this filament with the following results. The gas which is located between ~ 3 and 12 kpc to the west of the nucleus shows a complex velocity pattern. Figure 50 shows a typical spectrum of the $H\alpha + [N II]$ complex in this region. The lines are very wide and possibly split. For this gas we were able only to obtain a centroid for the $H\alpha + [N II]$ line complex in order to deter-

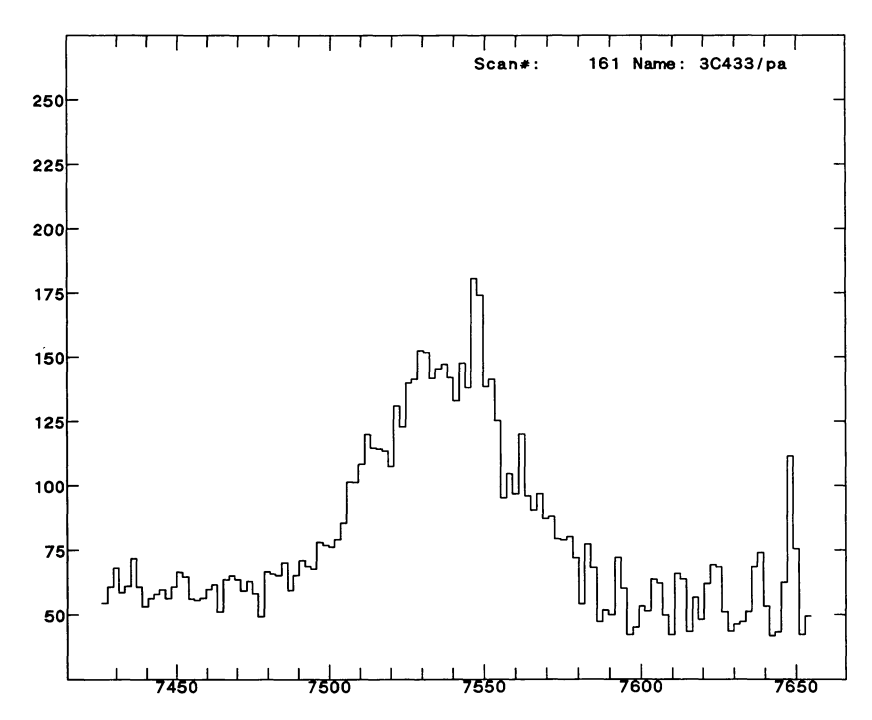


Fig. 50.—Spectrum of 3C 433 obtained at position angle 129, 3.5 pixels (3"01) east of the nucleus, showing the H α +[N II] complex

436 BAUM ET AL.

mine the velocity shifts. The velocities of the gas in this region appear disjoint (by -400 km s^{-1}) from the near nuclear gas. A velocity gradient from -400 km s^{-1} to near the velocity of the nuclear gas is seen along the 6 kpc extent of this segment of the nebula (i.e., a gradient of 67 km s⁻¹ kpc^{-1}) (see Fig. 41a, where we have plotted as crosses the relative velocities determined from the centroid of the H α + [N II] complex). Morphologically, there is no apparent difference between this part of the nebula and the remainder of the nebula. The messy velocity pattern exhibited by the gas might argue for an interaction of the radio source with the gas; however, the radio axis is misaligned from this region of the emission-line nebula by 36°.

To the southeast of the nebula, the velocities of the gas gradually decrease from the nuclear velocity to ~ -300 km s⁻¹. The line widths hover around ~ 400 km s⁻¹ (FWHM) in the inner regions of this part of the nebula, rising to above 600 km s^{-1} (FWHM) on the edges.

s) 3C 422

Our emission-line image shows nuclear line emission, a short extension of higher surface brightness emission along PA 36 (the radio axis), a surrounding circular region of diffuse emission with a diameter of ~ 4 kpc, and a curving tail of emission extending to the southeast. Along PA 36, our spectra show all velocities within 50 kpc of the nuclear velocity. Likewise, along PA 126, we find that within 1.5 kpc of the nucleus all velocities are within 50 km s⁻¹ of the nuclear velocity. Beyond 1.5 kpc, the velocities drop slightly to the southeast, reaching -100 km s^{-1} at a distance of 2.25 kpc, and rise slightly to the northwest, reaching ~ 100 km s⁻¹ at a distance of 2 kpc. Measured line widths are $\sim 300-400 \text{ km s}^{-1}$ (FWHM) throughout the nebula.

VI. SUMMARY

We have presented the results from an extensive program of long-slit spectroscopy of the extended emission-line regions around radio galaxies. In general, we do not find strong gradients in the H α to [N II] $\lambda 6583$ ratio within a source. Often there is a slight decline in this ratio with distance from the nucleus, but there are also a few cases in which the ratio rises rapidly in the very extended emission-line gas.

In some sources, the gas appears to be in rotation about the galaxy nucleus, with measured rotational velocities ranging from 100 to 325 km s⁻¹, and apparent flattenings of the rotation curves occurring at distances from 0.1 to 8 kpc from the nucleus. Frequently, the rotation curves appear to be asymmetrically situated with respect to the nuclear line-emitting gas, showing offsets of ~ 1 kpc, or ~ 60 km s⁻¹, with respect to the nuclear gas. The shift of the nuclear velocity from the mean velocity of the emission-line gas is sometimes in the sense of a redshift and sometimes in the sense of a blueshift.

In other sources we find that the near nuclear emission-line gas (within several kiloparsecs) shows no evidence for rotation, but that the velocities of the gas farther out are positive on one side of the nucleus and negative on the other. Finally, in others we find no evidence for rotational gradients across the nucleus but observe either all velocities within 50 km s⁻¹ of the velocity of the nuclear emission-line gas or velocities which vary greatly from the nuclear velocities, but in an unsystematic manner.

Measured line widths vary from 200 to 600 km s^{-1} (FWHM) on the nucleus. The line widths typically fall with increasing distance from the nucleus, although there are several potentially interesting exceptions to this pattern. Finally, in those sources where there is extended emission-line gas along the radio source axis we have been able to look for evidence that the gas and the radio source are interacting. While kinematic signs of such an interaction are present in a few sources, others show no evidence that the gas has been disturbed by the passage of the radio jet or the presence of backflowing radio plasma. These results will be discussed in more detail in a forthcoming analysis paper (Paper II).

REFERENCES

Baum, S. A., and Heckman, T. M. 1989 a, Ap. J., 336, 681.

1989b, Ap. J., 336, 702.

Baum, S. A., Heckman, T., Bridle, A., van Breugel, W., and Miley, G. 1988, Ap. J. Suppl., 68, 643 (Paper I).

Baum, S. A., Heckman, T., and van Breugel, W. 1989, in preparation

(Paper II).

Fosbury, R. A. E. 1986, in Structure and Evolution of Active Galactic Nuclei, eds. G. Giuricin, F. Mardirossian, M. Mezzetti, and M. Ramonella (Dordrecht: Reidel), p. 297.

Hansen, L., Noorgard-Nielsen, H. U., and Jorgensen, H. E. 1987, Astr. Ap. Suppl., 71, 465.

Heckman, T. M., Baum, S. A., van Breugel, W. J. M., and McCarthy, P.

1989, *Ap. J.*, **338**, 48. Heckman, T., Illingworth, G., Miley, G. K., and van Breugel, W. J. M.

1985, Ap. J., 299, 41.

McCarthy, P. 1988, Ph.D. thesis, University of California at Berkeley. Pierce, M. J., and Stockton, A. 1986, Ap. J., 281, 95.

Simkin, S. M. 1977, Ap. J., 217, 45.

Tadhunter, C. N., Fosbury, R. A. E., and Quinn, P. J. 1989, M.N.R.A.S., **240**, 225.

STEFI ALISON BAUM: Radiosterrenwacht, Postbus 2, 7990 AA, Dwingeloo, The Netherlands

TIMOTHY HECKMAN: Space Telescope Science Institute, 3700 San Martin Drive, Baltimore, MD 21218

WIL VAN BREUGEL: Lawrence Livermore National Laboratory, Institute of Geophysics and Planetary Physics, P.O. Box 808, L-413, Livermore, CA 94550